Journal of Computational Physics 530 (2025) 113908

Contents lists available at ScienceDirect

Journal of Computational Physics

journal homepage: www.elsevier.com/locate/jcp

An adaptive dual grid moment-of-fluid method for multiphase flows

Philippe Hergibo [a,b], Timothy N. Phillips [b], Zhihua Xie [a,*]

[a] School of Engineering, Cardiff University, Queen's Buildings, Cardiff, CF24 3AA, UK
[b] School of Mathematics, Cardiff University, Abacws, Cardiff, CF24 4AG, UK

ARTICLE INFO

MSC:
0000
1111

Keywords:
Multiphase flow
MOF method
Interface reconstruction
Adaptive mesh refinement
Dual grid

ABSTRACT

Simulations of multiphase flows serve as a crucial tool in understanding the complex fluid dynamics present in various natural and engineering phenomena. The moment-of-fluid (MOF) method is widely recognised for its accuracy and efficiency in capturing complicated topological changes, while extensions to the method have enabled fine structures like filaments to be resolved. In the essence of multiphase flows, the solution has emerged as an independently solvable numerical approach, thereby creating opportunities for more complex processing. A novel adaptive dual grid technique which utilises the moment-of-fluid method is proposed here (MOF-ADG). This framework allows the simultaneous adaptive resolution of fine interfacial details and the solution of the Navier-Stokes equations on a coarse grid. This novel approach is validated through several benchmark test cases including free surface flows like sloshing, the dam break problem and the Rayleigh-Taylor instability. Surface tension modelling is included and implemented for the rising bubble problem. The complex interfacial dynamics are captured accurately and the computational efficiency of this approach is demonstrated. Good agreement is obtained with existing numerical findings and experimental data in the literature.

1. Introduction

Multiphase flow, where two or more distinct phases coexist, is ubiquitous in various engineering applications, ranging from natural occurrences like river sediment transport to industrial applications like oil and gas extraction. The accurate representation of the interface between phases is paramount, ensuring that mass, momentum, and energy transfer are robustly and accurately simulated. The interface dynamics, governed by interfacial tension, wettability, and other physicochemical interactions, play a pivotal role in determining flow patterns, phase distribution, and heat and mass transfer rates. Thus, a precise characterisation of the interface is crucial for reliable and robust multiphase flow predictions.

Many numerical methods have been developed for this purpose, such as the volume-of-fluid (VOF) method [1,2] and the level-set (LS) method [3]. Generally, the VOF method conserves mass well while maintaining a sharp interface. However, for some complex flows the interface can become quite diffuse or smeared. The level-set method is well-suited for complex topologies, representing the interface implicitly through a distance function, however occasionally it encounters difficulties in conserving mass. The moment-

---

[*] Corresponding author.
E-mail address: zxie@cardiff.ac.uk (Z. Xie).

https://doi.org/10.1016/j.jcp.2025.113908
Received 27 February 2024; Received in revised form 25 February 2025; Accepted 2 March 2025

of-fluid (MOF) method [4] is an extension of the VOF method that overcomes some of its limitations and which enables improved interface reconstruction. The method allows subgrid reconstruction of features such as thin ligaments while maintaining mass conservation. The MOF method uses a mesh-based approach, transporting zeroth and first moments for interface reconstruction. Recent improvements in the MOF method have overcome problems associated with the spurious diffusion of material and artificial surface tension by reconstructing sharp and parabolic interfaces within a cell [5]. Some have found an analytical solution which overcomes the need to perform an optimisation step, initially for Cartesian grids [6] and then for tetrahedral cells [7]. Recent enhancements have reduced overall computational costs and broadened its complex applications [8–15]. The work of Desjardins et al. [16] attempts to overcome the limitation of the Continuum Surface Force (CSF) method in resolving filaments using a two-plane reconstruction technique in which a local construction of two distinct volume fraction fields is employed. This refinement enables the effective use of CSF even in cases where two interfaces coexist at sub-grid scale, as illustrated later in Fig. 3.

In the field of computational fluid dynamics (CFD), the dual grid method has emerged as a powerful method to enhance the accuracy and efficiency of the computation of complex flow phenomena by combining different solvers on different grids. In this context, the aim is to solve the Navier-Stokes and transport equations on separate grids. This method involves the use of two distinct grids: a primary grid that captures the overall flow domain (velocity-pressure) and a secondary or dual grid that focuses on interface reconstruction, scalar or mass transport, with attention on specific regions of interest, often where high gradients or intricate flow structures exist [17–20]. The contribution of Lentine et al. [20] is related to our work but uses a velocity projection on the coarse grid to maintain accuracy and computational efficiency and a level-set method for interface capturing. Generally, the convergence of the flow might have been achieved well before the interface attains its grid independence. Therefore, maintaining identical grid resolutions for both the Navier-Stokes and transport equations could prolong computational time excessively and unnecessarily [2,21]. One prominent approach within the dual grid framework is the overset grid method, in which multiple grids with different resolutions are overlaid on one another, allowing for localised refinement where necessary [22,23]. The overset grid method offers flexibility in grid generation, especially in complex geometries and facilitates dynamic simulations where grid movement is required. However, the method tends to focus on solid boundaries, whereas the primary focus in this paper is the dynamic deformation of interfaces. Indeed, in this context, the resolution of interfaces is improved by adaptivity.

Adaptive mesh refinement (AMR), particularly the quadtree approach, has gained significant traction in CFD due to its ability to dynamically adjust grid resolution to capture intricate flow features with high precision. The quadtree method subdivides the computational domain into quadrants, refining areas with high gradients or intricate flow details or coarsening regions with minimal variation. This ensures computational efficiency without compromising accuracy. The benefits of AMR include reduced computational cost, enhanced resolution in critical regions, and the ability to capture transient phenomena with high fidelity [24,25]. However, challenges persist, such as ensuring solution continuity across refined boundaries, increased algorithmic complexity, and potential difficulties in parallelisation [26–31]. Indeed, achieving refinement on a single AMR grid may induce large computation error. The efficiency on a single grid would be compromised with the novel unconstrained AMR framework for MOF methods [32].

Combining one technique or the other has been a subject of increasing interest in the numerical multiphase flow community. Oftentimes, most interface capturing/tracking methods have been either volume-of-fluid (VOF), level-set (LS) or even recently moment-of-fluid (MOF) methods. In these approaches, both Navier-Stokes and transport equations are solved on the same single grid. In these instances, some limitations appear such as the increased complexity in combining these numerical methods [33–36]. Dual grid techniques combined with VOF [2] or LS [20,37,38] methods have been developed but usually on fixed grids. Some have included adaptivity with the level-set method for combustion [39]. However, despite recent advances in MOF methods, the integration of dual grid techniques with adaptive mesh refinement, has not yet been achieved.

The objective of this study is to extend the dual grid method complexity using adaptivity. The novel contribution of this paper is the development of a moment-of-fluid adaptive dual grid (MOF-ADG) method for multiphase flows. This variant of the MOF method is computationally efficient and is immensely promising for CFD applications involving complex multiphase flows. This innovative approach incorporates the combination of the most recent and complex research topics in a straightforward fashion. Significantly reducing computational expense while enhancing accuracy has emerged as a recent focus in the CFD community, thus expanding the horizons of research applications. This combination harnesses the strengths of both methods, offering flexibility and efficiency with dual grids and dynamic adaptability via AMR. This paper focuses on the seamless integration of these techniques, ensuring solution consistency across overlapping and refined grids. The synergy of dual grid and AMR not only enhances computational efficiency but also elevates the accuracy and robustness of flow predictions in complex engineering applications. A known challenge in multiphase flow simulations arises when multiple buoyant bubbles are underresolved on the velocity grid but are well captured on the interface grid. In such cases, if the bubbles are homogeneously distributed throughout the computational domain, they will fail to rise, as the coarse velocity grid cannot adequately resolve the necessary buoyancy-driven motion [40]. This results in significant inaccuracies in the computation of the rise velocity due to its interpolation from a coarse grid, leading to errors compared to a more standard approach with a uniform fine grid. This limitation is inherent to many numerical approaches, including our method.

This paper is organised as follows. Section 2 describes the governing equations as well as the MOF method and recent developments and improvements on a fixed grid. The adaptive mesh refinement scheme and its structure together with the dual grid implementation are presented in Section 3. In Section 4, results and analysis of several benchmark problems are presented. Discussion on the efficiency of the method is discussed in Section 5. Finally, some concluding remarks are made in Section 6.

2. Numerical framework

2.1. Governing equations

The multiphase dynamics of an incompressible fluid are described by the Navier-Stokes equations which comprise the continuity and momentum equations for each material. These equations are given by

$$\nabla \cdot \mathbf{u} = 0 \tag{1}$$

$$\frac{\partial(\rho \mathbf{u})}{\partial t} + \nabla \cdot (\rho \mathbf{u} \otimes \mathbf{u}) = -\nabla p + \nabla \cdot \left[\mu \left(\nabla \mathbf{u} + \nabla \mathbf{u}^T\right)\right] + \rho \mathbf{g} + \mathbf{f} \tag{2}$$

respectively, where $\mathbf{u}$ is the velocity vector, p the pressure, t the time, $\mathbf{g}$ the gravitational force and $\mathbf{f}$ external forces (e.g. surface tension or excitation force). The parameters ρ and μ are the density and dynamic viscosity, respectively.

In the context of multiphase flows, Equations (1) and (2) are solved throughout the computational domain using a weighted description of density and viscosity that is phase-dependent. In particular, these material properties are specified by

$$\rho = F\rho^{\mathrm{a}} + (1-F)\rho^{\mathrm{b}}, \tag{3}$$

$$\mu = F\mu^{\mathrm{a}} + (1-F)\mu^{\mathrm{b}}, \tag{4}$$

respectively, with the two fluids designated as ‘a’ and ‘b’ and F representing the volume fraction of material ‘a’ within a cell. The advection equation for F is discussed and solved in Section 2.4.

2.2. Navier-Stokes solver

The governing equations are discretised on a staggered mesh using the finite volume method and solved using a Cartesian grid-based fluid flow solver [41]. This approach involves dividing the computational domain into a structured Cartesian grid, where the fluid flow solver utilises staggered grid arrangements. Fig. 1 highlights the arrangement of velocity and pressure on the staggered grid.

The finite volume method, applied to this staggered grid configuration, ensures the conservation of mass and momentum by integrating the governing equations over control volumes. This combined strategy not only simplifies the representation of complex geometries but also enhances numerical stability, making it a widely employed and effective approach in CFD.

Consider a control volume Ω that has an arbitrary domain, the surface of the control volume is S and the unit outward normal vector to the face of the domain is $\boldsymbol{n}$. The Navier-Stokes equations (1) and (2) can be recast into an integral form as below,

$$\int_S \mathbf{u} \cdot \boldsymbol{n} \mathrm{d}S = 0 \tag{5}$$

$$\int_\Omega \frac{\partial \rho \mathbf{u}}{\partial t} \mathrm{d}\Omega + \int_S (\rho \mathbf{u} \cdot \boldsymbol{n}) \mathbf{u} \mathrm{d}S = \int_\Omega -\nabla p \mathrm{d}\Omega + \int_S \mu \left(\nabla \mathbf{u} + \nabla \mathbf{u}^T\right) \mathrm{d}S + \int_\Omega (\rho \mathbf{g} + \mathbf{f}) \mathrm{d}\Omega. \tag{6}$$

For the temporal discretisation, a first-order backward Euler method is used for time derivatives, which lead to an implicit scheme for the momentum equation. In the spatial discretisation, advection terms are handled using a high-resolution scheme for accuracy and monotonicity, while pressure and diffusion term gradients are computed using a central difference scheme [42]. Let $\mathbf{u}_{i,j}$ denote the face-centred horizontal and vertical velocities within a grid cell and let $p_{i,j}$ represent the pressure which is evaluated at the cell centre (shown in Fig. 1). When substituting all the discretised terms into the momentum equation (6), an implicit equation with the following structure for determining the velocity at location P can be derived

$$a^{\mathbf{u}}_{\mathrm{P}} \mathbf{u}^{n+1}_{\mathrm{P}} = \sum a^{\mathbf{u}}_{\mathrm{nb}} \mathbf{u}^{n+1}_{\mathrm{nb}} + b^{\mathbf{u}}_{\mathrm{P}} + A_{\mathrm{f}}(p_{\mathrm{P}} - p_{\mathrm{nb}}), \tag{7}$$

where $a^{\mathbf{u}}$ is the coefficient for the momentum equation and A_{f} is the surface area of control volume faces, the subscripts P and $\mathrm{nb} = \mathrm{E}, \mathrm{W}, \mathrm{N}, \mathrm{S}$ denote the variables in the present and neighbouring cells (shown in Fig. 1), respectively, and $b^{\mathbf{u}}_{\mathrm{P}}$ is the source term.

The SIMPLE (Semi-Implicit Method for Pressure-Linked Equations) algorithm [43] is used for pressure-velocity coupling in this study. For the initial pressure or latest iteration of pressure distribution p^*, the discretised momentum equations can be solved together with under-relaxation technique to produce the fluid velocities $\mathbf{u}^*$, which satisfy the momentum equation (7)

$$\frac{a^{\mathbf{u}}_{\mathrm{P}}}{\alpha_{\mathbf{u}}} \mathbf{u}^*_{\mathrm{P}} = \sum a^{\mathbf{u}}_{\mathrm{nb}} \mathbf{u}^*_{\mathrm{nb}} + b^{\mathbf{u}}_{\mathrm{P}} + \frac{1-\alpha_{\mathbf{u}}}{\alpha_{\mathbf{u}}} \mathbf{u}^0_{\mathrm{P}} + A_{\mathrm{f}}(p^*_{\mathrm{P}} - p^*_{\mathrm{nb}}), \tag{8}$$

where $0 < \alpha_{\mathbf{u}} < 1$ is the under-relaxation factor ($\alpha_{\mathbf{u}} = 0.7$ is used here) and $\mathbf{u}^0_{\mathrm{P}}$ is the value from previous iteration.

To obtain the pressure correction, the updated fluid velocities are substituted into the discretised continuity equation (5) and the resulting pressure correction equation for p' has the following form

$$a^p_{\mathrm{P}} p'_{\mathrm{P}} = \sum a^p_{\mathrm{nb}} p'_{\mathrm{nb}} + b'_{\mathrm{P}}, \tag{9}$$

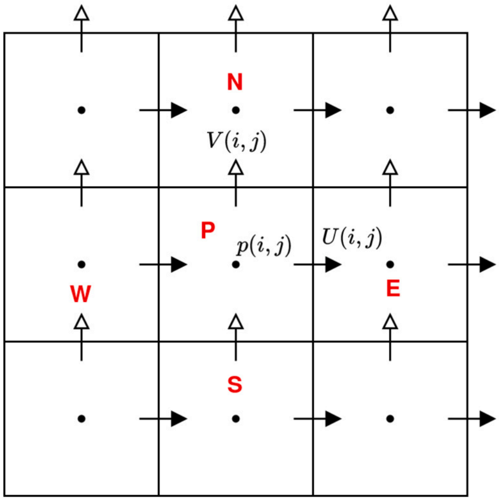

Fig. 1. Staggered grid arrangement on a 3×3 grid. The black circles represent the cell-centred pressure $p(i,j)$. The plain arrows represent face-centred horizontal velocities $U(i,j)$ and the hollow arrows face-centred vertical velocities $V(i,j)$. The red letters correspond to the present cell P and its neighbouring cells N, S, W, E. (For interpretation of the colours in the figure(s), the reader is referred to the web version of this article.)

where a^p is the coefficient for the continuity equation and the term b'_{P}, called the mass residual, is the left-hand side of the discretised continuity equation calculated in terms of the updated fluid velocities $\mathbf{u}^*$.

After solving the pressure corrections p', the final solutions for the pressure and velocity values in the control volume are updated as

$$p = p^* + \alpha_p p', \tag{10}$$

$$\mathbf{u} = \mathbf{u}^* + \mathbf{u}', \tag{11}$$

where

$$\mathbf{u}' = \frac{\alpha_{\mathbf{u}} A_{\mathrm{f}}}{a_{\mathrm{P}}^{\mathbf{u}}}(p'_{\mathrm{P}} - p'_{\mathrm{nb}}), \tag{12}$$

and $\alpha_p = 1 - \alpha_{\mathbf{u}}$ is the under-relaxation factor for the pressure.

2.3. Surface tension model

In cases where interfacial forces play a significant role, surface tension must be considered. A continuum surface force model [44] is incorporated into the Navier-Stokes equations to represent surface tension. This force $\mathbf{f}_\sigma$ can be described as:

$$\mathbf{f}_\sigma = \sigma \kappa \mathbf{n} \delta \tag{13}$$

where σ is the surface tension coefficient, $\mathbf{n}$ is the interface normal, $\kappa = -\nabla \cdot \mathbf{n}$ is the interfacial curvature and δ is the Dirac delta function. We use $\delta = |\nabla F|$ and $\mathbf{n} = \frac{\nabla F}{|\nabla F|}$ to address the surface tension modelling as a function of the volume fraction.

The interfacial normal $\mathbf{n}$ is discretised using a smoothed volume fraction function. The curvature term is discretised by approximating the normal at cell faces and its surrounding neighbouring values. It can be expressed as:

$$\kappa_{i,j} = -\left(\frac{n^x_{i,j} - n^x_{i-1,j}}{\Delta x} + \frac{n^y_{i,j} - n^y_{i,j-1}}{\Delta y} \right) \tag{14}$$

where the superscripts x and y corresponds to the horizontal and vertical components of the normal $\mathbf{n}$ on the fixed coarse grid, Δx and Δy represent the fixed coarse grid sizes in the horizontal and vertical directions, respectively.

2.4. Interface capturing method

The transport of the interface is controlled by the advection equation for the volume fraction F as

$$\frac{\partial F}{\partial t} + \mathbf{u} \cdot \nabla F = 0 \tag{15}$$

where $\mathbf{u}$ is the velocity field.

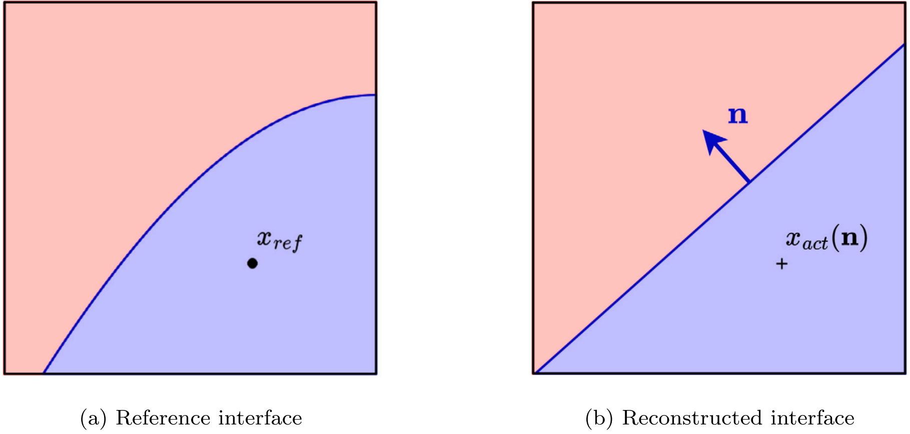

(a) Reference interface

(b) Reconstructed interface

Fig. 2. Reference and reconstructed interface using the MOF method: $\mathbf{x}_{ref}$ is the reference centroid, $\mathbf{x}_{act}(\mathbf{n})$ the reconstructed centroid, and $\mathbf{n}$ is the normal to the reconstructed interface.

The ability to accurately model interfaces and conserve mass as well as the ease of implementation for complex problems are key technical reasons to adopt the new emerging interface capturing method that is the MOF method. By accurately handling complex geometries, dynamic boundaries, and fluid-solid interactions, the MOF method enhances numerical stability and fidelity, making it a valuable tool in a diverse range of applications, such as free surface flows [45–47], droplet/bubble dynamics [36,48], and fluid-structure interactions [49].

Initially, the MOF method identifies fluid interfaces. Subsequently, it computes the moments of the materials present within each computational cell and aims to maintain the shape of the interface accurately. This includes calculating the zeroth moment (volume fraction) and the first moment (material centroid). The interface can then be reconstructed without the need for neighbouring cell information [4,6,50]. Not requiring information from neighbouring cells to reconstruct interfaces is a great advantage for the adaptive dual grid technique as other methods might have difficulty in achieving the same level of complexity. The MOF method can be viewed as the constrained optimisation problem:

$$\min \left|\mathbf{x}_{ref} - \mathbf{x}_{act}(\mathbf{n})\right| \tag{16}$$

subject to the constraint

$$\left|F_{ref} - F_{act}(\mathbf{n})\right| = 0 \tag{17}$$

where F_{ref} and F_{act} are the reference volume fraction (zeroth moment) and the reconstructed volume fraction, respectively, $\mathbf{x}_{ref}$ and $\mathbf{x}_{act}(\mathbf{n})$ are the reference centroid (first moment) and the reconstructed centroid, respectively, $\mathbf{n}$ represents the normal vector used in piecewise linear interface calculation. Fig. 2 depicts the reference interface of any shape, curved or linear, where the centroid of the material considered is $\mathbf{x}_{ref}$. The reconstructed interface is a linear interface with an outward pointing normal $\mathbf{n}$, and the polygon that is reconstructed has the reconstructed centroid $\mathbf{x}_{act}(\mathbf{n})$.

Additionally, efforts have been made to incorporate the MOF method into symmetric reconstruction, adaptive mesh refinement and multi-material techniques, enabling more precise simulations with reduced computational costs [8–12]. Another significant enhancement involves the integration of the MOF method with machine learning and artificial intelligence for improved interface capturing and prediction. These innovations collectively contribute to the MOF method's growing applicability [13].

Filaments within the VOF method [51] and MOF method [14,15] have played a significant contribution in its progress by enabling more accurate and detailed representations of fluid interfaces. Innovations in filament manipulation and reconstruction have led to improvements in its wide use.

Fig. 3 displays three examples of the MOF method to incorporate additional features. Multi-material, filaments, unconstrained refinement are significant benefits of these enhancements to the MOF method. Fig. 3(a) illustrates how the minimisation nature of the MOF method is exploited by trying all possible reconstruction scenarios (nested dissection) when three different materials coexist in a cell. Using symmetric reconstruction improves the efficiency and accuracy of interface reconstruction by minimising the combination of the two materials considered in the desired reconstruction. The symmetric reconstruction process requires the minimisation of the following functional to determine the normal $\mathbf{n}$ to the interface

$$E_c^{sym}(\mathbf{n}) = \left|\mathbf{x}_{ref} - \mathbf{x}_{act}(\mathbf{n})\right| + \left|\mathbf{x}_{ref}^{rem} - \mathbf{x}_{act}^{rem}(\mathbf{n})\right| \tag{18}$$

where the superscript *rem* corresponds to the remaining material under consideration.

In similar fashion, Fig. 3(b) shows a filament reconstruction. Two interfaces coexist within a cell, indeed two conglomerates of the same material (white background) are evaluated as not being adjacent to each other. One of these conglomerates is considered to

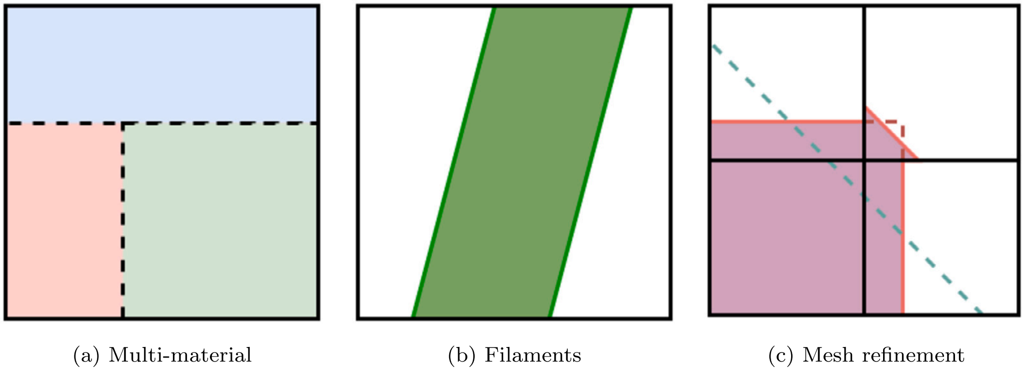

Fig. 3. Evolution of complexity of reconstruction using the MOF method. (a) and (b) using a symmetric nested dissection, (c) using standard MOF for refinement around sharp edges. The red dashed line represents the reference interface, while the green dashed line represents the MOF reconstruction without filament.

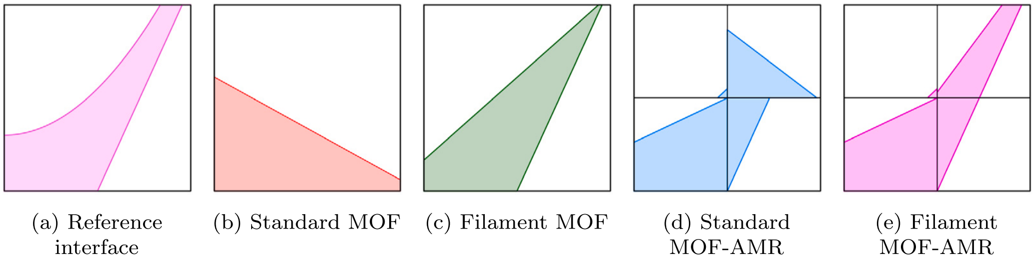

Fig. 4. Example of complex reconstruction using the MOF-AMR method in which the aim is to reconstruct a curved filamentary interface: (a) reference interface, (b) fixed grid reconstruction using standard MOF which highlights the limitation of this method, (c) fixed grid reconstruction using a filament MOF in which the linear interface is reconstructed with a certain error, (d) reconstruction using standard MOF with one level of refinement which still shows the limitations of standard reconstruction, (e) reconstruction using a combination of filament MOF and MOF-AMR which enables to reconstruct a linear interface while mitigating the error of the curved interface.

be a fictitious material, leading to a multi-material case scenario. All possible scenarios are tested when reconstructing the first then the second interface. The final solution minimises all centroids in the cell using the minimisation function

$$E = \sqrt{\sum_{i=1}^{n} \left|\mathbf{x}_{ref}(\psi_i) - \mathbf{x}_{act}(\psi_i)\right|^2} \tag{19}$$

where $\mathbf{x}_{ref}(\psi_i)$ is the reference centroid of material ψ_i and $\mathbf{x}_{act}(\psi_i)$ is its reconstructed centroid. The fictitious material is reassigned to its original material after reconstruction.

Fig. 3(c) illustrates the refinement process in which a cell is subdivided into four subcells when the reconstruction error is larger than a user-defined criterion, usually $10^{-9}\Delta x(lev)$. Here $\Delta x(lev)$ defines the subcell size at level *lev*. Since the MOF method uses piecewise linear interpolation to calculate the interface, it struggles to reconstruct sharp edges within a cell. Therefore, refining these is very helpful in maintaining highly accurate sharp interfaces. The red dashed line denotes the reference interface formed by a rectangular shape encompassing four subcells. The reconstructed interface before refinement is depicted as a green dashed line, highlighting the significant error incurred in reconstruction.

In Fig. 4, the comprehensive integration of the three diverse and complex MOF examples mentioned above is combined. These complexities, namely symmetric multi-material reconstruction, filament approach, and unconstrained adaptive grid refinement, collectively contribute to the evolution of MOF methods. A closer examination of the refinement process reveals a structure, incorporating one distinct level of refinement, in which one subcell contains a filament reconstruction. This implies a refinement strategy, in which each region undergoes a detailed filament detection procedure.

3. Adpative dual grid

Adaptive dual grid is an innovative approach in the field of fluid dynamics, designed to address the computational challenges associated with complex and evolving flow phenomena. This method uses the power of adaptivity to dynamically refine grids in response to changes in local flow characteristics, enabling higher resolution in regions of interest. By intelligently allocating computational resources on two grids, one solving the velocity-pressure coupling and the other resolving the dynamic interface, the adaptive dual grid technique offers significant advantages in simulating a wide range of fluid dynamics problems over fixed dual grids or a single adaptive grid.

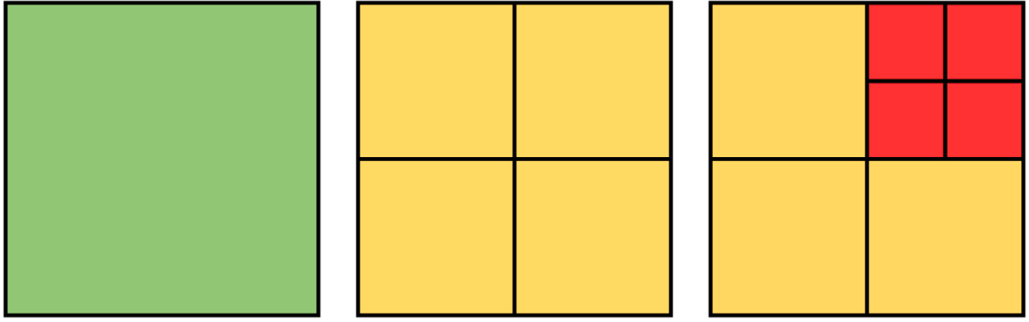

(a) Level 0
$is = 1; js = 1$

(b) Level 1
$is = 1:2; js = 1:2$

(c) Level 2
$is = 1:4; js = 1:4$

Fig. 5. Structure and indexing of the novel quadtree approach. Green cell corresponds to level 0 (L0), yellow cells to level 1 (L1) and red cells to level 2 (L2).

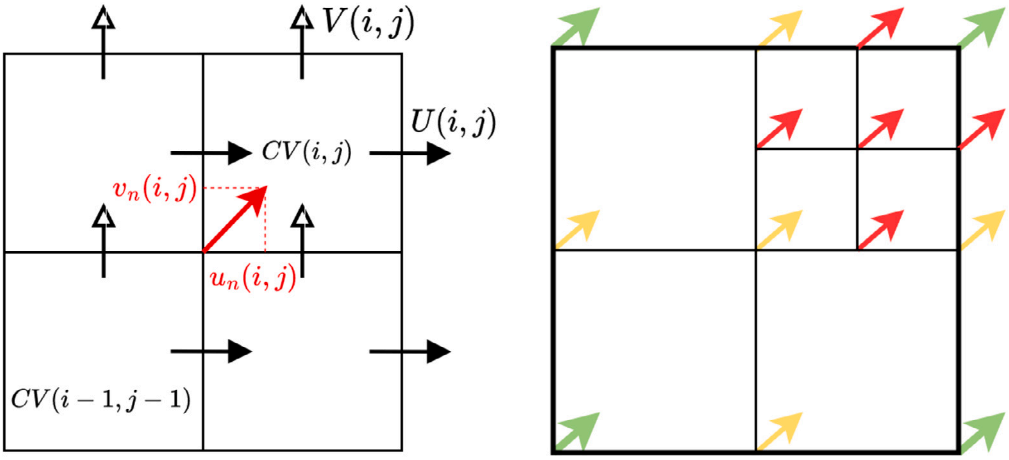

(a) Node velocity interpolated in a control volume denoted $CV(i,j)$. Plain black arrows are horizontal velocities U, hollow black arrows are vertical velocities V, both face-centered. The red arrow denotes the node velocity with components in horizontal and vertical directions u_n and v_n, respectively.

(b) Node velocity interpolation when refining grid for level 0 (green arrows), level 1 (yellow arrows) and level 2 (red arrows).

Fig. 6. Visual schematic of the interpolation of node velocity from the fluid solver fixed grid to the MOF-ADG grid. All other velocities when subsequently refining the grid are interpolated from the four fixed grid nodes.

3.1. Adaptive mesh refinement

The unconstrained quadtree adaptive mesh refinement method [9] is a sophisticated numerical technique employed to enhance accuracy and computational efficiency. A hierarchical data structure, referred to as a quadtree, is used where the domain is repeatedly divided into subcells based on a user-defined criterion. Unlike constrained methods, which follow the 2:1 refinement rule, the unconstrained approach allows for irregular grid adaptations, making it particularly well-suited for capturing complex flow features efficiently.

In the novel yet simplified quadtree mesh approach [32], an arbitrary cell is denoted by (i, j, is, js), where (i, j) signifies the base mesh coordinates. Subsequently, the subcell indices is and js are related to the desired level, lev, of refinement. To access children cells, a logic based on the parent cell's index parity is employed, where children subcell indices are given by $(2is-1, 2is)$ when the parent index is even and $(is, is+1)$ when the parent index is odd. This logical scheme is applicable up to level 2 and is applicable in both the horizontal and vertical directions. Mathematically, cells and subcells at their finest refinement level are contained in a set Φ_{lev} including non-overlapping subsets Φ_0, Φ_1 and Φ_2. Fig. 5 highlights the refinement structure and indexing of the hierarchy. In this example, the green cells are level 0 (L0), the yellow subcells are level 1 (L1) and the red subcells are level 2 (L2). This example clearly demonstrates that the red subcells indices are $(3:4, 3:4)$.

The triggering of refinement in the context of the MOF method employed here uses the centroid error as the primary criterion. This approach considers the reconstruction error as an effective gauge of the accuracy of the reconstruction, which encompasses

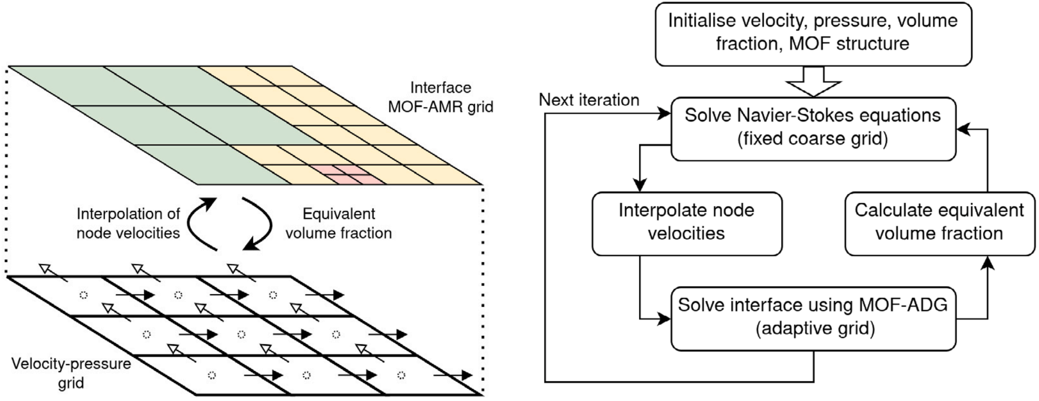

(a) (b)

Fig. 7. (a) Structure and (b) flowchart of the adaptive dual grid method. (a) Top grid is the interface MOF-AMR grid using the same colouring scheme described in the previous section. Bottom grid is the fluid solver grid, where dashed circles represent cell-centred pressure and volume fraction $F_{NS}(i,j)$, plain arrows represent horizontal velocities U and hollow arrows vertical velocities V, both face-centred. Communication between grids is required for velocities and volume fractions.

the material centroid error, including the fictitious material in filament scenarios. Notably, the refinement criterion in this study is normalised by the cell size. More details can be found in Hergibo et al. [32].

3.2. Dual grid method

The dual grid method involves the addition of a secondary grid together with the primary grid, which allows for a refined resolution of complex flow features. Conserving computational resources is critical in the context of MOF methods since the optimisation component of the method can be expensive. By adapting the grid resolution locally, the adaptive dual grid method aims to enhance the precision and fidelity of numerical simulations in accurately predicting fluid dynamics.

Due to the unconstrained nature of our novel AMR structure, calculating fluxes through different levels of refinement on a single AMR grid may be necessary for velocity, pressure and volume fraction variables. Therefore, the dual grid aspect comes naturally. Indeed in numerical multiphase flow simulations, the velocity-pressure coupling and volume fraction are solved independently. The adaptive dual grid method stems from the difference in resolution needed for accurate interface representation. Reasons to use an adaptive dual grid approach rather than a single AMR grid include facilitating parallel computation, limiting the complexity of the flux calculations, utilising the convergence rates for different parts of the numerical scheme and the unconstrained nature of this approach.

The velocity-pressure coupling on a coarse grid facilitates the overall understanding of the flow. Concurrently, the interface dynamics are effectively resolved on an AMR grid. The exchange between the two grids is facilitated through smooth communication of vital information. The first part of the communication is from the fluid solver on a fixed coarse grid to the interface MOF-AMR grid, in which the node velocities needed to advect the interface are interpolated from the base grid for the Navier-Stokes solver. Indeed, the fluid solver is composed of face-defined velocities U and V, in the horizontal and vertical direction of a control volume, respectively. The interpolation is applied linearly on a uniform Cartesian grid with i and j indices as follows

$$\begin{aligned} u_n(i,j) &= \frac{U(i-1,j-1)+U(i-1,j)}{2} \\ v_n(i,j) &= \frac{V(i-1,j-1)+V(i,j-1)}{2} \end{aligned} \tag{20}$$

where u_n and v_n are the horizontal and vertical velocities at the bottom left corner node of the control volume used in the MOF context. In the fluid solver, the pressure and volume fraction are cell-centred. Fig. 6(a) shows how node velocities are spatially interpolated for a single control volume, in addition to its directional components. Fig. 6(b) considers the node velocity interpolation when refinement is triggered in the dynamic procedure. These velocities are required during the material advection part. More details can be found in Hergibo et al. [32].

The second part of the communication process exchanges information about volume fraction between the MOF-AMR grid and the fixed coarse grid used for the fluid solver in order to solve the system of discretised equations. The exchange is performed in the following way. Communication to the coarse grid is carried out using the equivalent volume fraction as follows

$$F_{NS}(i,j) = \sum_{lev} \sum_{is,js \subset \{\Phi_{lev}\}} \frac{F_{ADG}(i,j,is,js,lev)\,|\Omega|\,(lev)}{|\Omega|\,(0)} \tag{21}$$

where $F_{NS}(i,j)$ denotes the volume fraction used on the flow solver grid, Φ_{lev} is the set of cells/subcells and is, js and lev are indices in the AMR structure for each level of refinement and $|\Omega|\,(lev)$ corresponds to the subcell area. It is crucial to note that if a cell has not been refined then level 0 remains. In this case, the above relationship is simplified as follows

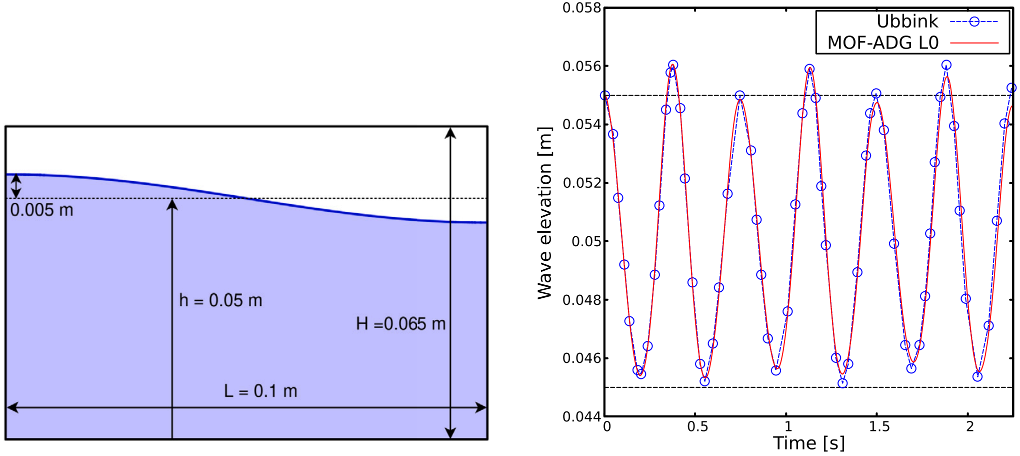

(a) Schematic of the domain and initial condition (b) Evolution of the wave elevation

Fig. 8. Inviscid sloshing case: (a) schematic of the initial conditions, (b) evolution of the wave elevation compared with the predictions of Ubbink [52].

$$F_{NS}(i,j) = F_{ADG}(i,j,1,1,0) \tag{22}$$

Fig. 7 serves as an illustrative snapshot of the effective communication and integration between the two grids. The depiction encapsulates the exchange of data and information that is fundamental to the success of the adaptive dual grid method. The coordination, as seen with the flowchart, is essential for maintaining accuracy and coherence in the numerical simulation.

When surface tension forces are significant, additional interaction between the two grids is required to maintain the correct physical behaviour and to ensure accuracy of the flow features. The interaction happens on two levels. As described above, the velocity field is communicated to the secondary grid (AMR grid) while the volume fraction is transferred back to the primary grid (Navier-Stokes fixed coarse grid). In addition, the curvature is calculated on the secondary grid and interpolated to communicate an equivalent coarse grid value. In this paper, the equivalent fixed grid volume fraction is summed using all the subcells volume fraction, including potential mass redistribution. This equivalent volume fraction is smoothed and used to determine the cell face normal and therefore curvature.

4. Results

4.1. Sloshing

4.1.1. Free sloshing of inviscid fluids

In this section, sloshing, the study of uncontrolled oscillatory motion of a liquid within a container, is examined. Typically caused by external forces or perturbations, complex topological changes are created in the free surface. We first consider the inviscid sloshing, where no viscosity is applied resulting in no damping of the fluid motion.

For the inviscid sloshing case, we replicate the configuration used by Ubbink [52] for an algebraic VOF method. The rectangular tank has length $L = 0.1$ m and height $H = 0.065$ m. The initial wave is a half cosine of amplitude 0.005 m with the still water level at rest at $h = 0.05$ m. Fig. 8(a) shows the domain and initial condition with a half cosine wave. The ratio of densities of the fluids is 1000 and both viscosities are set to 0.

At the initial stage, the liquid exhibits a half wave length perturbation. As time progresses, characteristic wave patterns are formed. In this case, the period is given by

$$P = \frac{2\pi}{\sqrt{gk\tanh(kh)}} \tag{23}$$

where $g = 9.8$ ms^{-2} is the acceleration due to gravity, h is the still water height and k the wave number defined by $k = \pi/L$. Fig. 8(b) displays the wave elevation at the left boundary in physical units for the initial six periods only using a level 0 grid. The waves are not damped as this case is inviscid. The frequency aligns with the theoretical frequency. The wave elevation exhibits different behaviour for even and odd periods, related to wave modes. In both cases the amplitudes match the predictions of Ubbink [52].

4.1.2. Free sloshing of viscous fluids

The second part considers the influence of viscosity on the sloshing motion by varying the Reynolds number, resulting in damping of the wave elevation over time to different degrees. In this instance, we make comparison with the predictions of Liu and Lin [53]. In this setting the dimensions of the container and the initial condition are changed. The tank has length of $L = 1$ m and height of $H = 0.65$ m. The initial wave is a full wavelength and its amplitude is set to 0.01 m, while the water depth is maintained around 0.5 m. Fig. 9 shows the computational domain and initial condition.

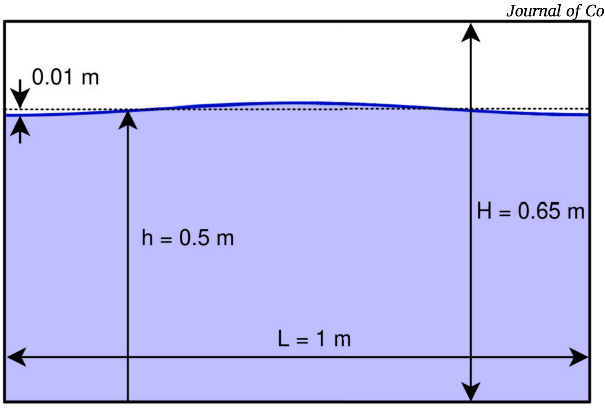

Fig. 9. Schematic of the tank dimensions and initial condition.

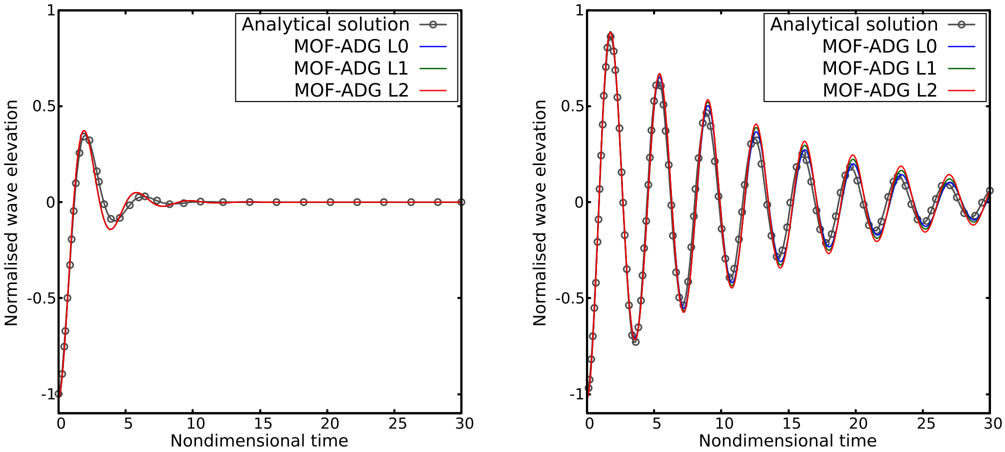

(a) $Re = 20$

(b) $Re = 200$

Fig. 10. Evolution of water level at the left boundary using the MOF-ADG method with a 40×26 base grid compared with the analytical solution for (a) $Re = 20$, (b) $Re = 200$.

Two scenarios are studied: $Re = 20$ and $Re = 200$, where Re is defined by

$$Re = \frac{\rho h \sqrt{gh}}{\mu} \tag{24}$$

and ρ and μ are the density and dynamic viscosity of water, respectively. The air-water density ratio is maintained as per the inviscid case. The viscosity ratio is kept constant while studying different Reynolds number. In both cases, three levels of grid resolution were implemented using the novel MOF-ADG method. The first one corresponds to a fixed grid, level 0 (L0), the second has one level of refinement (L1) and finally, the last has two levels of refinement (L2). The simulation time is extended to 30 units, where time is multiplied by $\sqrt{g/h}$ to obtain a dimensionless time. The timestep used across different refinements is constant.

Fig. 10 presents the normalised wave elevation at the left boundary as a function of the nondimensional time. For both cases, $Re = 20$ and $Re = 200$, numerical predictions on all three grids are compared with the analytical solution provided by Liu and Lin [53] and Wu et al. [54]. The characteristic oscillatory behaviour reveals a gradual reduction in wave amplitude. Notably, the decay rate of the wave is more pronounced for a smaller Reynolds number. In both situations, the wave elevation at the left boundary matches favourably the analytical solution. Note that for a low Reynolds number the adaptive dual grid method exhibits very similar behaviour irrespective of the levels of refinement while a higher Reynolds number exhibits a slight discrepancy in wave elevation when using one or two levels of refinement.

Fig. 11 depicts a natural sloshing sequence at various time intervals revealing the dynamic behaviour and evolution of liquid movement within a tank when $Re = 200$. The coarse grid is composed of a 40×26 arrangement of Cartesian cells. As time progresses, subsequent figures capture the agitation at $T = 1.7$, $T = 3.55$ and $T = 30$. Note that for these two cases, the wave period is different from the inviscid case. These figures provide a comprehensive visual representation, illustrating the dynamics of sloshing using the MOF-ADG method.

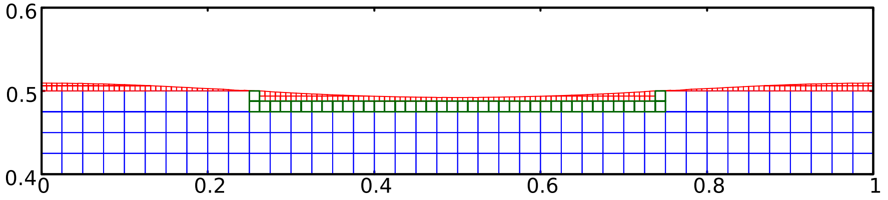

(a) $T = 1.7$

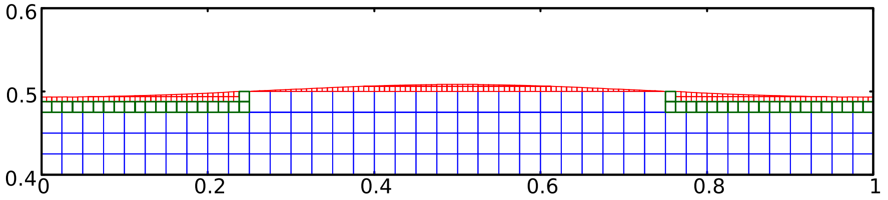

(b) $T = 3.55$

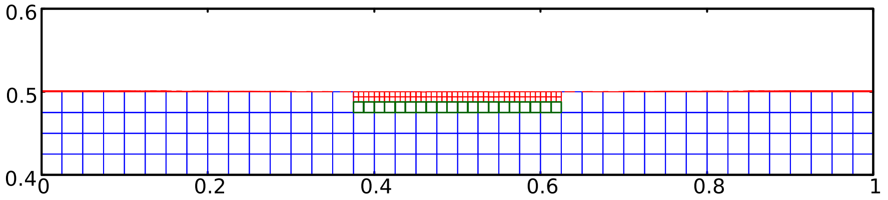

(c) $T = 30$

Fig. 11. Evolution of water level within the tank when $Re = 200$. Zoom is carried out on the interface to highlight the performance of the MOF-ADG method. The base grid (L0) is composed of 40×26 Cartesian cells. Blue depicts level 0 (L0), green level 1 (L1) and red level 2 (L2).

4.1.3. Viscous sloshing under horizontal excitation

In this section, the sloshing of a liquid in a 2D rectangular tank that is horizontally agitated is assessed. The excitation occurs periodically, with velocity $\mathbf{u}_{exc} = [-A\omega\cos(\omega t), 0]$, where A is the displacement amplitude and ω denotes the angular frequency of the excitation. Within the momentum equation (2), this excitation is provided as an external force $\mathbf{f}_{exc}$ in addition to gravity forces i.e.

$$\mathbf{f}_{exc} = -\rho \, \frac{d\mathbf{u}_{exc}}{dt} \tag{25}$$

The parameters and dimensions of the tank are similar to the free sloshing case above. The mesh used to generate the results is finer to better track the complex dynamics. The notable difference is the initial condition. In such a scenario, the natural frequency of the fluid in the tank is expressed as $\omega_0 = \sqrt{\pi g \tanh(\pi h)}\ \mathrm{s}^{-1}$ [53]. In the following test case, the free surface is initially at rest in the tank at a new height $h = 0.175$ m. For this test case, the amplitude and frequency are specified as follows: $A = 0.06$ m and $\omega = 2.0\omega_0$.

This case is showcasing the ability of the MOF-ADG method to handle complex dynamics. Fig. 12 shows the evolution of the interface, which increases in complexity until the forming jet falls onto the free surface. Note that thanks to two levels of refinement, the thin jet is not breaking up and maintains a sharp interface. The first jet with the motion of the tank then creates a secondary jet that is thinner. This means that breakup is likely, however the observations show that the breakup occurs only with two levels of refinement, highlighting that the method is capable of effectively capturing subgrid features. The series of snapshots captured during the simulation offer a visual narrative of the dynamic topology of the interface. It also highlights the interaction taking place within the domain near the wall boundaries.

4.2. Dam break

Demonstrating its significance as a benchmark problem in multiphase flow simulations, the phenomenon of dam breaking encompasses intricate dynamics, including high-impact pressures, surface fragmentation, and the formation of water jets, among others. The investigation presented in this section focuses on dam breaking and aims at replicating the experimental work of Zhou et al. [55] and Buchner [56]. The computational domain consists of a rectangular tank measuring 3.22 m in length and 1.8 m in height. The lower-left corner accommodates the water phase, with a reference density of 1000 kg/m^3, occupying an area of 1.2 m in width and $H = 0.6$ m in height. The air medium is characterised by a reference density of 1.29 kg/m^3. Fig. 13 offers a visual schematic of the domain. Time is nondimensionalised by $\sqrt{g/H}$, pressure by $\rho g H$ and height by H.

Validating the numerical simulations of a dam break event against experimental and numerical data in the literature is vital in demonstrating the reliability of the method. Fig. 14 shows a sequence of three snapshots following the collapse of a dam under the

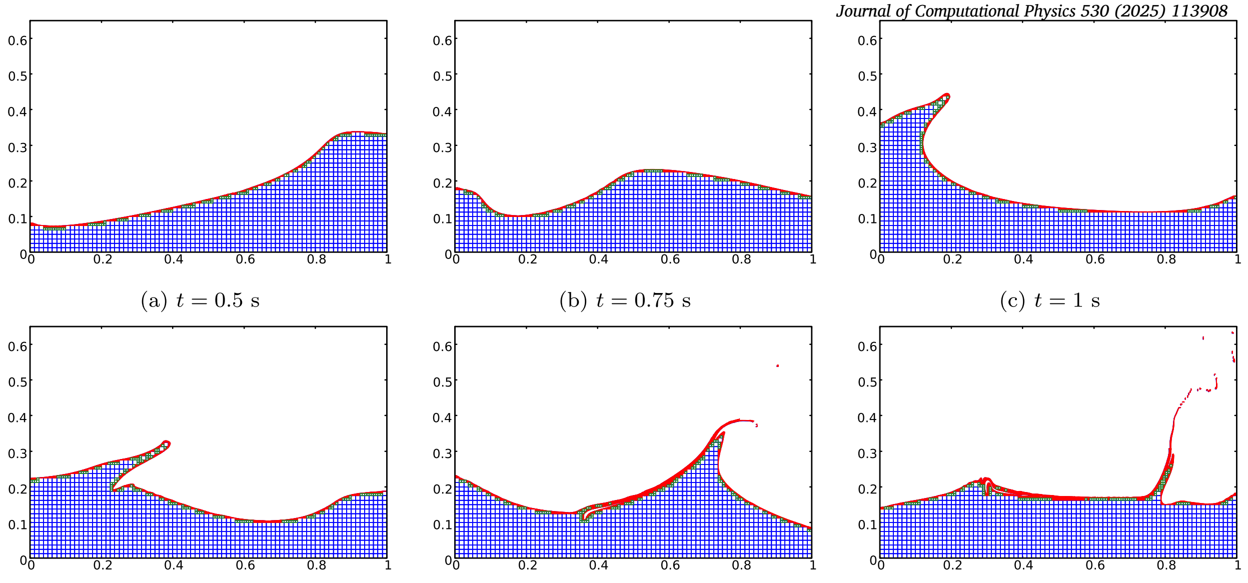

(a) $t = 0.5$ s (b) $t = 0.75$ s (c) $t = 1$ s

(d) $t = 1.25$ s (e) $t = 1.5$ s (f) $t = 1.75$ s

Fig. 12. Snapshots of the evolution of the air-water interface during horizontal excitation (sloshing) of a tank initially at rest and with $A = 0.06$ m and $\omega = 2.0\omega_0$ using the MOF-ADG with two adaptive levels of refinement.

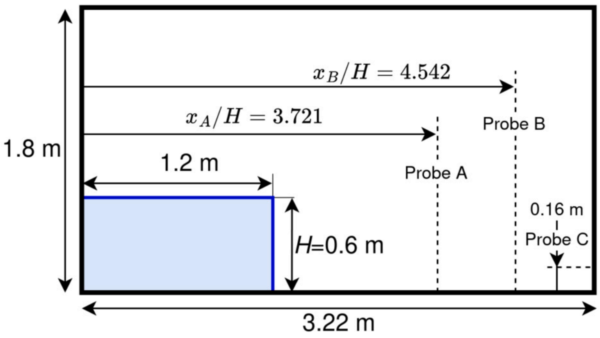

Fig. 13. Schematic of the domain, initial condition and location of probes A, B and C, which are used as instrumental validation.

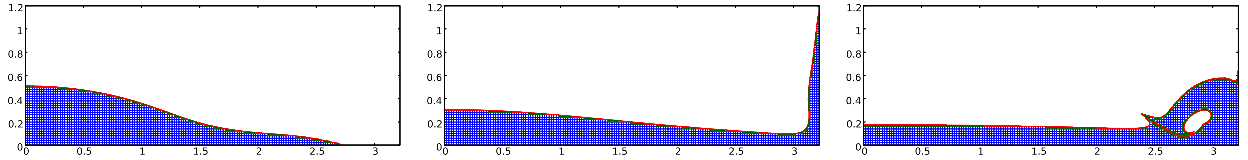

(a) $T = 2$ (b) $T = 4$ (c) $T = 6.2$

Fig. 14. Evolution of the air-water interface for the dam break problem using the MOF-ADG method with two levels of refinement.

influence of gravity. Snapshots show two levels of refinement where the base grid is composed of 161×90 Cartesian cells. When the dam breaks the surge position advances rapidly. This is followed by a strong vertical motion after the water impacts the right-hand wall. Eventually, the liquid falls back on itself creating a cavity. Using the filament MOF method and a coarse timestep, the snapshot reveals a thin air film that does not enclose the cavity completely.

Our present adaptive dual grid MOF method preserves detailed phenomena, such as water splashing and the formation of flow jets. Fig. 15 shows the results of our present method for level 0, 1 and 2 and comparison is made with the level-set method and SPH methods provided by Colicchio et al. [57]. The air cavity is well captured and enclosed using MOF-ADG (L0) method, while still containing a few ‘bubbles of air’. Other numerical methods also capture the air cavity but a large discrepancy occurs in predicting its location. The level-set method creates a large bridge of coalescence and a small cavity whilst the SPH method creates a large cavity. The associated jet also shows a significant difference between the three methods. Note that the process of interface refinement tends to create a thin film of air, rather than fully enveloping the cavity.

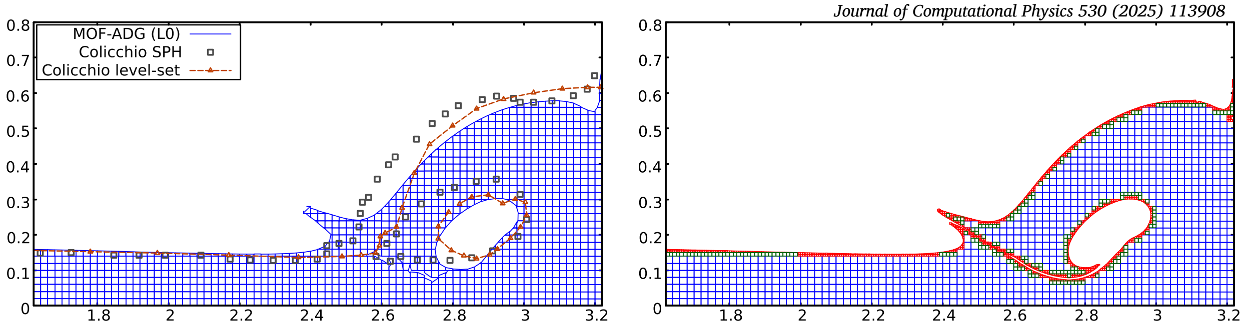

(a) Comparison of the MOF-ADG (L0) with SPH & level-set

(b) Zoom on the interface using MOF-ADG (L2)

Fig. 15. Comparison of the air-water interface for the MOF-ADG, level-set and SPH methods at $T = 6.2$. Interface with level 0 is in blue, level 1 in green and level 2 in red.

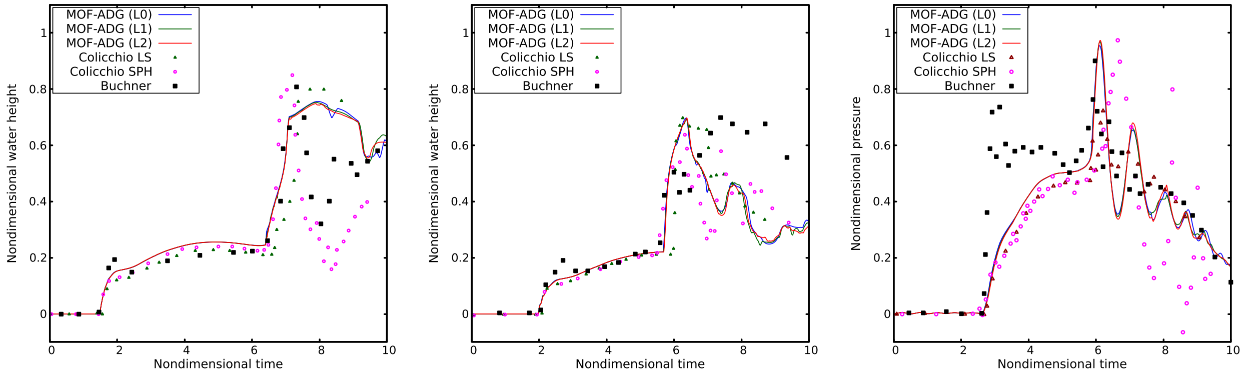

(a) Water height measurement at probe A.

(b) Water height measurement at probe B.

(c) Pressure measurement at probe C.

Fig. 16. Water height and pressure measurement analysis using MOF-ADG method compared to level-set and SPH methods from Colicchio [57] and experimental work from Buchner [56].

Fig. 16 illustrates the temporal evolution of water height and pressure at three locations. These probes were used in the early experiments performed by Zhou et al. [55] and Buchner [56]. Probe A is located at $x_A/H = 3.721$, probe B at $x_B/H = 4.542$ along the horizontal axis accounting for water height evaluation. Probe C is located at the right hand wall at a height of 0.16 m.

While the experimental and numerical trends exhibit a satisfactory level of agreement for water height measurements until $T = 6.5$, a notable disparity emerges throughout the second part of the simulation and the water level peak seems to be underestimated. The initial pressure rise agrees well with other numerical methods but there is a delay in attaining its peak value compared to experimental work. Note that the different resolutions of the MOF-ADG method exhibit nearly overlapping trends. In conclusion, there is a relatively limited level of agreement between the computational results and the experimental data which may be due to the pressure transducer location or variations in the water front propagation velocity. Challenges in achieving measurement repeatability have been previously documented leading to inconclusive findings when comparing with experimental data [55]. However, most of the numerical methods seems to show good agreement with each other.

4.3. Rayleigh-Taylor instability

This well-known instability is a phenomenon that emerges when gravity causes a heavy fluid initially at rest on top of a lighter fluid to deform the interface between them. In our study, we adopt the same configuration used in previous investigations [17,58,59]. The rectangular domain is $[0, d] \times [0, 4d]$ and the interface is initially perturbed with a sinusoidal waveform of amplitude $0.1d$. The Atwood ratio A, a measure of the density difference between the heavier and lighter fluids, is defined by

$$A = \frac{\rho_H - \rho_L}{\rho_H + \rho_L} \tag{26}$$

where the subscripts H and L, respectively, denote a heavy and light fluid. Time is nondimensionalised by $\sqrt{d/Ag}$, and surface tension and turbulence effects are ignored in this study. In this test case we set $A = 0.5$.

We conduct computations using three cases for our present MOF-ADG method with different levels of refinement while using the same finest Cartesian grid size. Therefore for these computations, the timestep is the same. The coarsest grid is 32×128 with

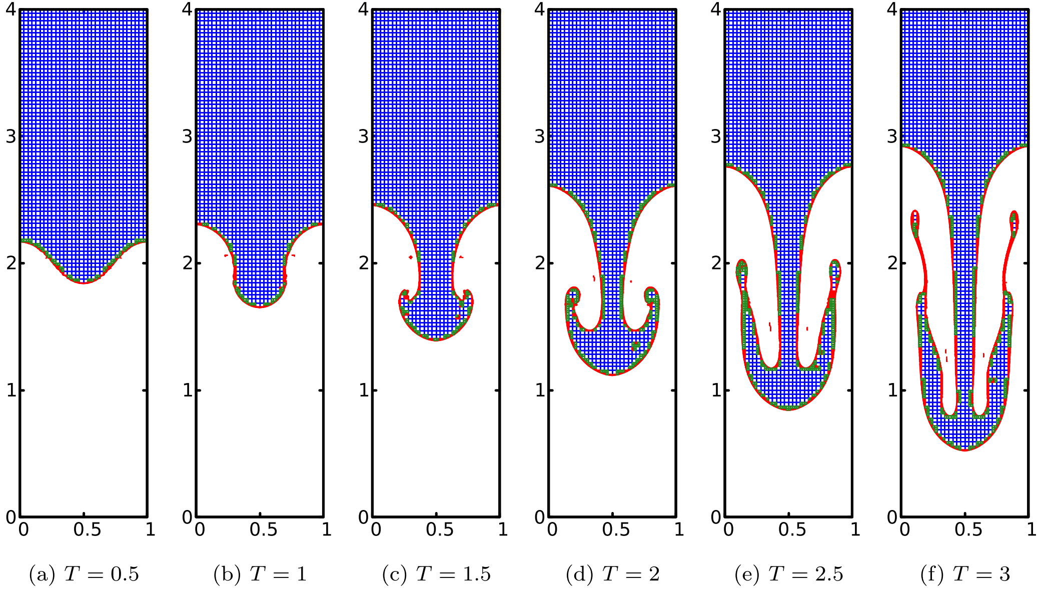

Fig. 17. Snapshots showing the evolution of the interface between the heavy fluid (blue) and the light fluid (white) using the novel MOF-ADG method with a 32×128 base grid with two levels of refinement. T is nondimensional time.

two refinement levels (L2), the medium grid is 64×256 (L1) and the finest grid is 128×512 (L0), respectively. Fig. 17 shows a sequence of snapshots revealing the evolution of the interface, where the heavy fluid falls into the lighter fluid. The early stages of the deformation of the interface exhibit a 'mushroom' like shape, then thinner structures begin to appear as the material becomes increasingly deformed. Some 'bubbles'/'droplets' appear in the material and are highlighted with the colour scheme of the refinement.

Fig. 18 highlights the refined reconstruction of the interface during deformation at a nondimensional time of $T = 3.5$ for the three cases. We observe that the 'mushroom' shape formation during the spike penetration is reconstructed well. The interface remains sharp and exhibits very limited diffusion. Many filaments are present, but grid convergence of these structures is elusive. To the best of the authors' knowledge, such a late stage of simulation with a coarse grid and subgrid structures has not been achieved.

In order to investigate the robustness and performance of the MOF-ADG method, we provide some insights into its performance in Fig. 19. Acceptable mass conservation is achieved throughout the simulation (Fig. 19(b)). Reducing the timestep would improve mass conservation even further but at a greater computational cost. The Courant number is not a limiting factor in our MOF approach. Two fundamental variables, cell count and filament subroutine count are shown on a common plot in Fig. 19(c). The filament subroutine count cycles through the domain and iterations during the dynamic process in order to evaluate how many times the filament reconstruction subroutine has been called. Since two interfaces are reconstructed within a cell, it is important to understand its potential influence on the computational cost. The juxtaposition between cell count and filament count allows for a clear and concise comparison of the influence of these outputs offering potential correlations with runtime. Moreover, the last figure (Fig. 19(d)) offers a crucial evaluation of the relative runtime performance of each principal component of the computation. The total runtime is compared with respect to the time of the shortest simulation, shown as a percentage, with the rest providing a more expensive computation. The AMR and reconstruction subroutines are responsible for a major part of the interface capturing procedure as per Hergibo et al. [32]. The time spent in these subroutines is added together across all iterations and each value in the AMR and reconstruction histogram corresponds to the percentage of time shared between them. It clearly shows a significant time spent in the AMR at level 2 while having nearly the same amount of filament to reconstruct. As reported in Hergibo [32], in many instances a single level of refinement is the most efficient approach.

4.4. 2D rising bubble case

The 2D rising bubble test case is examined in this section. In this problem, a bubble with radius $r = 0.25$ is initially placed at the point $(0.5, 0.5)$ within a rectangular domain $[0, 1] \times [0, 2]$. Slip boundary conditions are applied on the left and right walls, while no-slip conditions are enforced at the top and bottom. Following Hysing et al. [60], we focus on the case where surface tension causes the formation of thin trailing filaments. The density ratio between the liquid and gas phases is 1000, and the viscosity ratio is 100. The surface tension coefficient is 1.96 Nm^{-1}, and the gravitational acceleration is 0.98 ms^{-2}. Surface tension is incorporated through an additional term in the external force balance, as outlined in Section 2.3.

Fig. 20 presents a visual depiction of the evolution of the shape of the bubble using the adaptive dual grid method for a coarse fixed grid and the highest level of refinement. The simulation is carried out until $t = 3$ s.

In this study, we use the same finest grid size. Therefore, three different grid resolutions are run until $t = 3$ s, respectively: 120×240 with level 0, 60×120 with level 1 and 30×60 with level 2. Fig. 21 presents the numerical results for the three grid scenarios. The

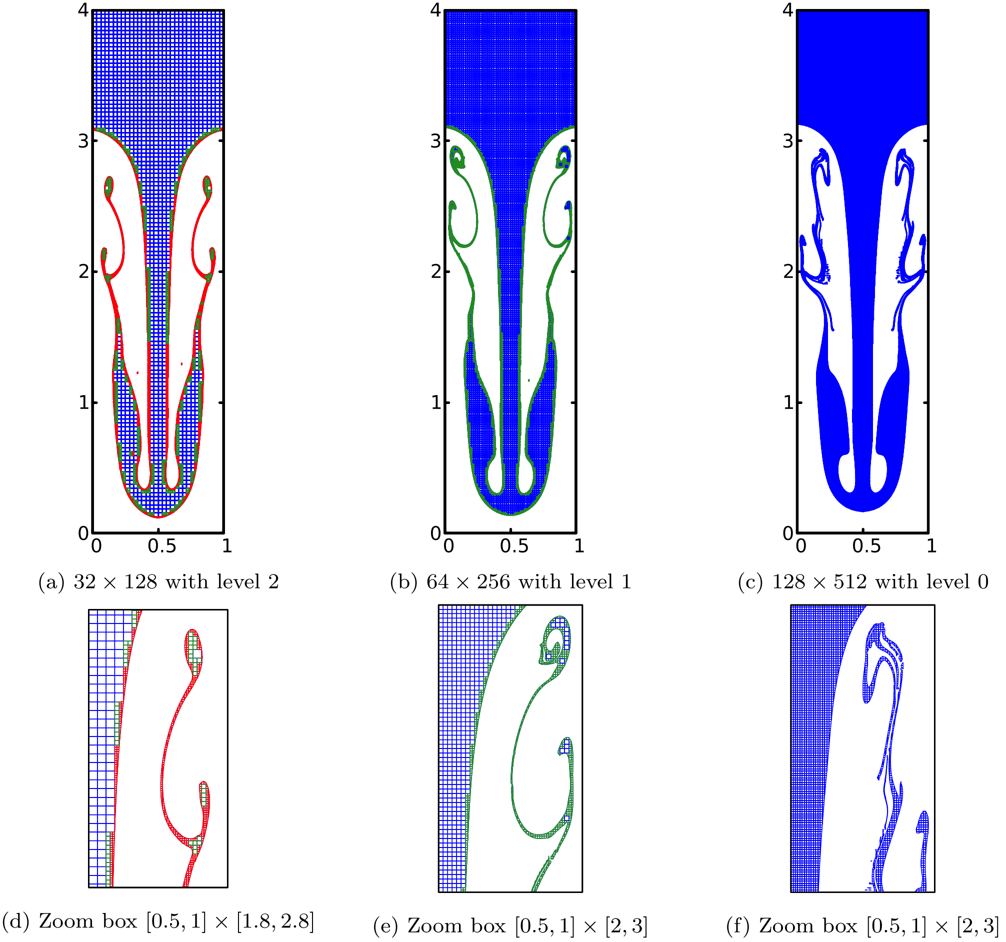

(a) 32 × 128 with level 2
(b) 64 × 256 with level 1
(c) 128 × 512 with level 0

(d) Zoom box [0.5, 1] × [1.8, 2.8]
(e) Zoom box [0.5, 1] × [2, 3]
(f) Zoom box [0.5, 1] × [2, 3]

Fig. 18. Snapshots of the Rayleigh-Taylor instability for the MOF-ADG method at $T = 3.5$ for the same finest level of refinement. In the zoom boxes, blue denotes level 0, green level 1 and red level 2.

simulation results indicate the formation of a thicker filament for the case with the most refinement. Moreover, the satellite bubble seems to be located at a slightly different location. The dynamics of the bubble tend to follow its base grid behaviour. In addition, the model demonstrates slightly better mass conservation properties for the most refined case, capped within −0.7%, along with a less circular satellite bubble. A shorter runtime is observed for the finest refinement compared to a less refined case, which is expected as fewer cells are resolved both for the fixed coarse grid flow solver and the adaptive interfacial grid.

Fig. 22 compares the bubble profile at $t = 3$ s on the finest grid with profiles from the literature [60,61] and the evolution of the centre of mass and bubble rise velocity. As expected, there are differences in the resolution of the filament: the TP2D (Transport Phenomena in 2D) method [60] shows a clear breakup, while the conservative level-set method of Doherty et al. [61] maintains the satellite bubble within the main bubble. The evolution of the centre of mass agrees well with these two references. The rise velocity shows slight deviations from the reference values but remains within the expected physical bounds of the problem.

5. Discussion on the efficiency of the MOF-ADG method

5.1. Rayleigh-Taylor instability

The MOF-ADG method framework offers a compromise between accuracy and runtime. It achieves this by using dual grid benefits and also refining regions of interest. It naturally reduces the overall number of cells used in a computation compared to a uniform grid or a single AMR grid. Typically, in AMR practices, runtime increases as the number of refinement levels increase, resulting in decreased error or a more precise region of interest.

However, in the context of the MOF method, regions experiencing high deformation may be able to be reconstructed effortlessly using filaments while maintaining a reasonable computational cost. Consequently, one can assess the accuracy of various levels of a MOF-ADG method using the filament procedure. Note that a filament reconstruction with a higher base resolution but a lower level of refinement may be equivalent to a lower base resolution reconstruction but with a higher level of refinement.

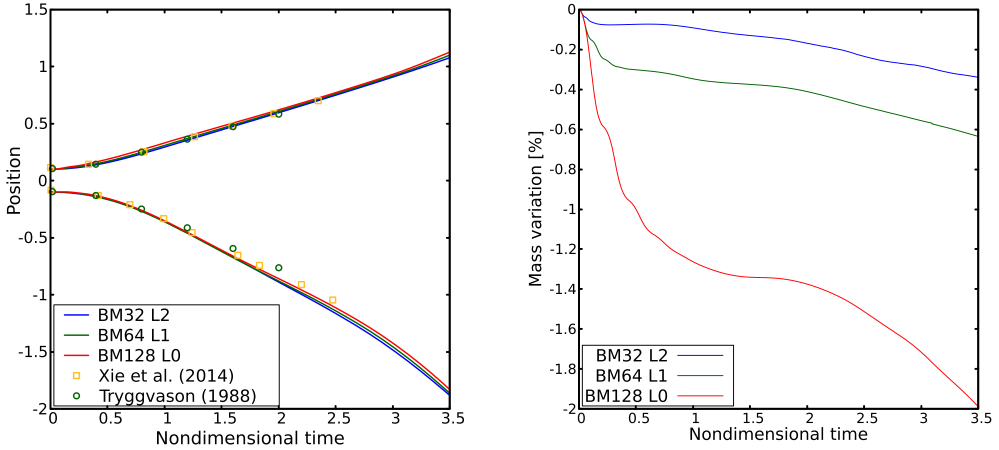

(a) Evolution of the spike position

(b) Mass variation

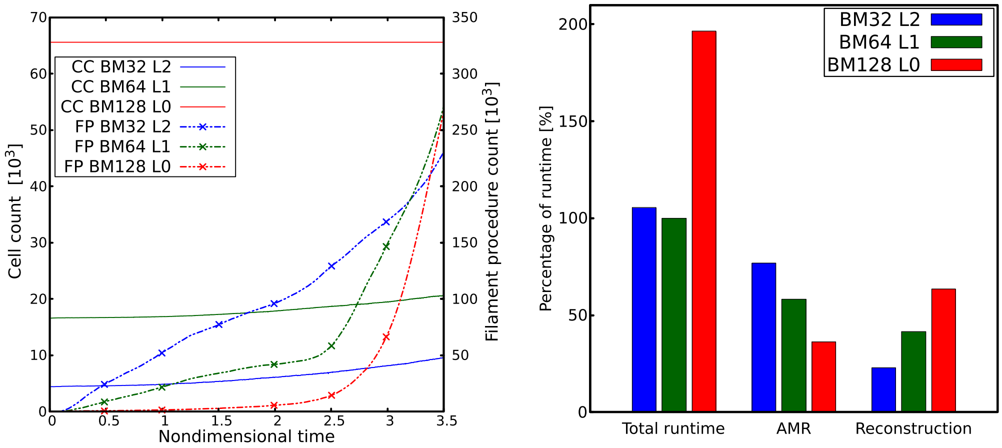

(c) Cell & filament count

(d) Runtime

Fig. 19. Detailed analysis of several numerical data of the MOF-ADG method. BM stands for base mesh. CC stands for cell count and FP for filament procedure. 100% total runtime is based on the shortest simulation.

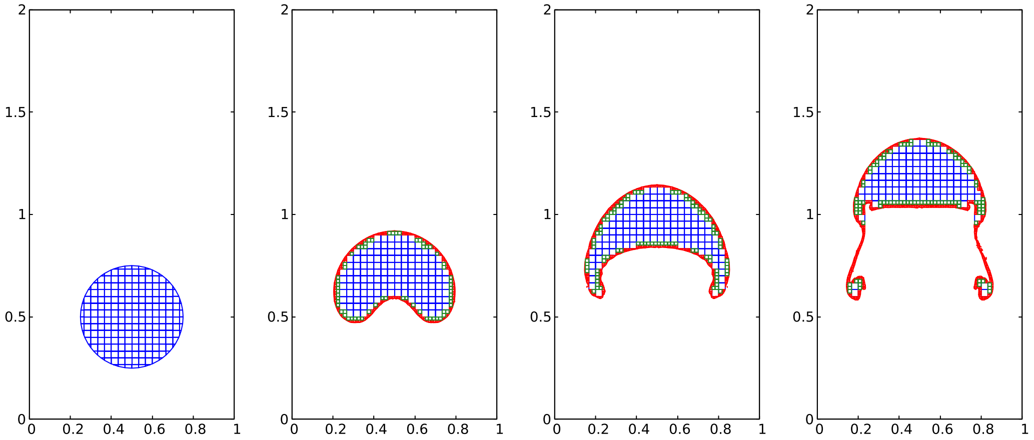

(a) $t = 0$ s

(b) $t = 1$ s

(c) $t = 2$ s

(d) $t = 3$ s

Fig. 20. Evolution of the rising bubble from $t = 0$ to $t = 3$ s using an adaptive dual grid method including surface tension modelling and two levels of refinement.

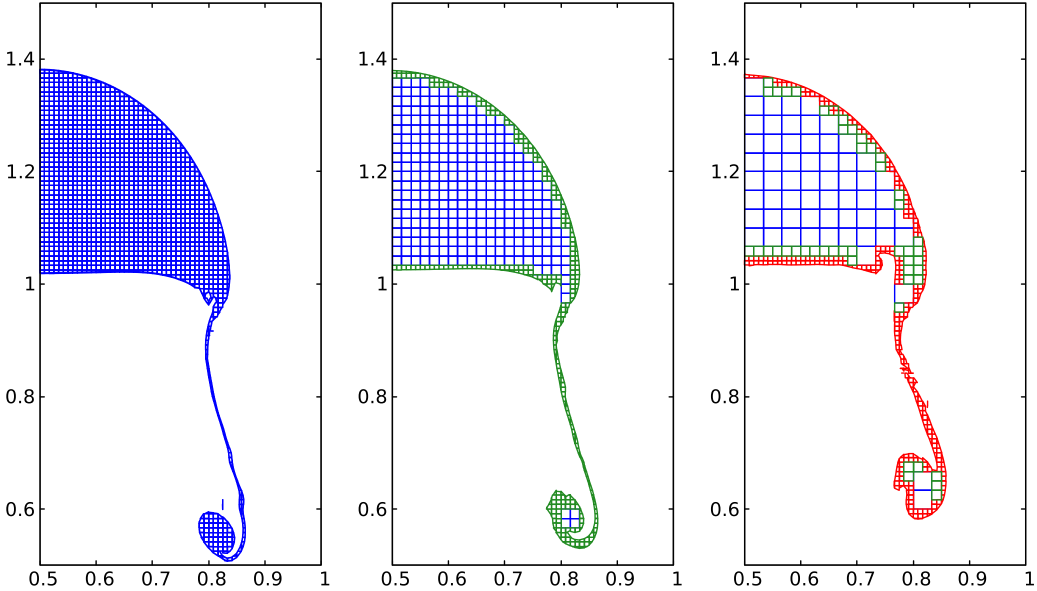

(a) 120 × 240 with level 0
Runtime : 2718 s

(b) 60 × 120 with level 1
Runtime : 638 s

(c) 30 × 60 with level 2
Runtime : 345 s

Fig. 21. Bubble profile at $t = 3$ s using the filament MOF-ADG method for three grid resolutions using the same finest grid size.

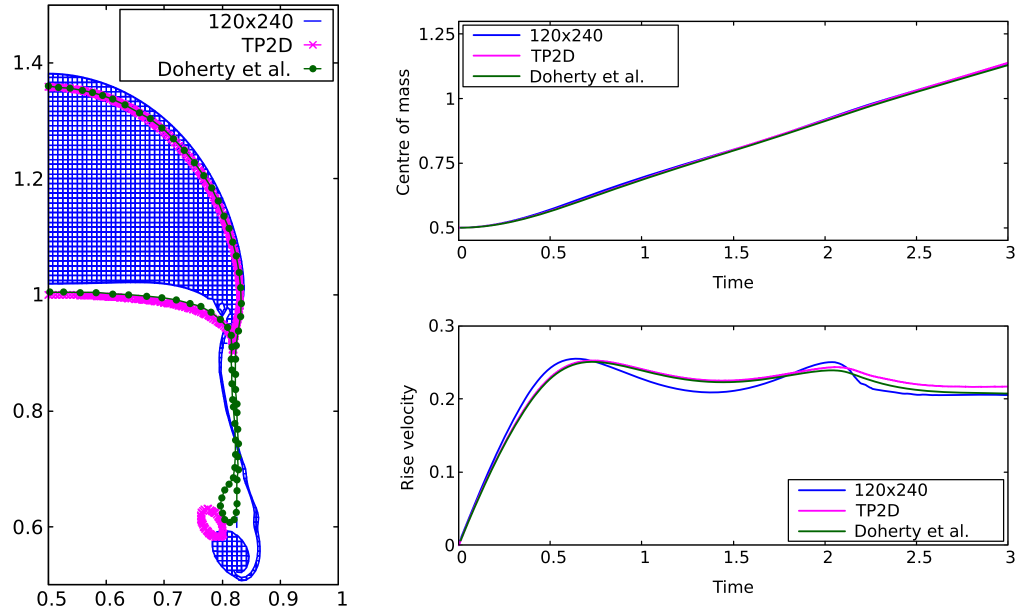

Fig. 22. Comparison of the predicted centre of mass, rise velocity and bubble shape with TP2D [60] and Doherty et al. [61].

This section aims to provide insights into the trade-off between refinement and error using the Rayleigh-Taylor instability problem. The timestep remains constant across all test cases, therefore, comparing runtime alone may not provide a comprehensive understanding of efficiency. The first set of cases uses a 32×128 grid with level 0, 1 and 2 and a standard reconstruction. The second set of cases uses the same resolution but with a filament reconstruction.

Fig. 23 demonstrates that, in general, standard reconstruction does not provide a great deal of improvement and two levels of refinement are needed. However, for such extreme filamentary cases, a coarse grid and one level of refinement does not prevent the breakup of filaments, even when enabling filament reconstruction. Eventually, two levels of refinement are necessary to achieve an acceptable degree of precision, although using a standard reconstruction gives a poor result. The zoom provided shows the standard MOF method with two levels of refinement is on the edge of breaking up whereas the filament MOF method shows a smoother

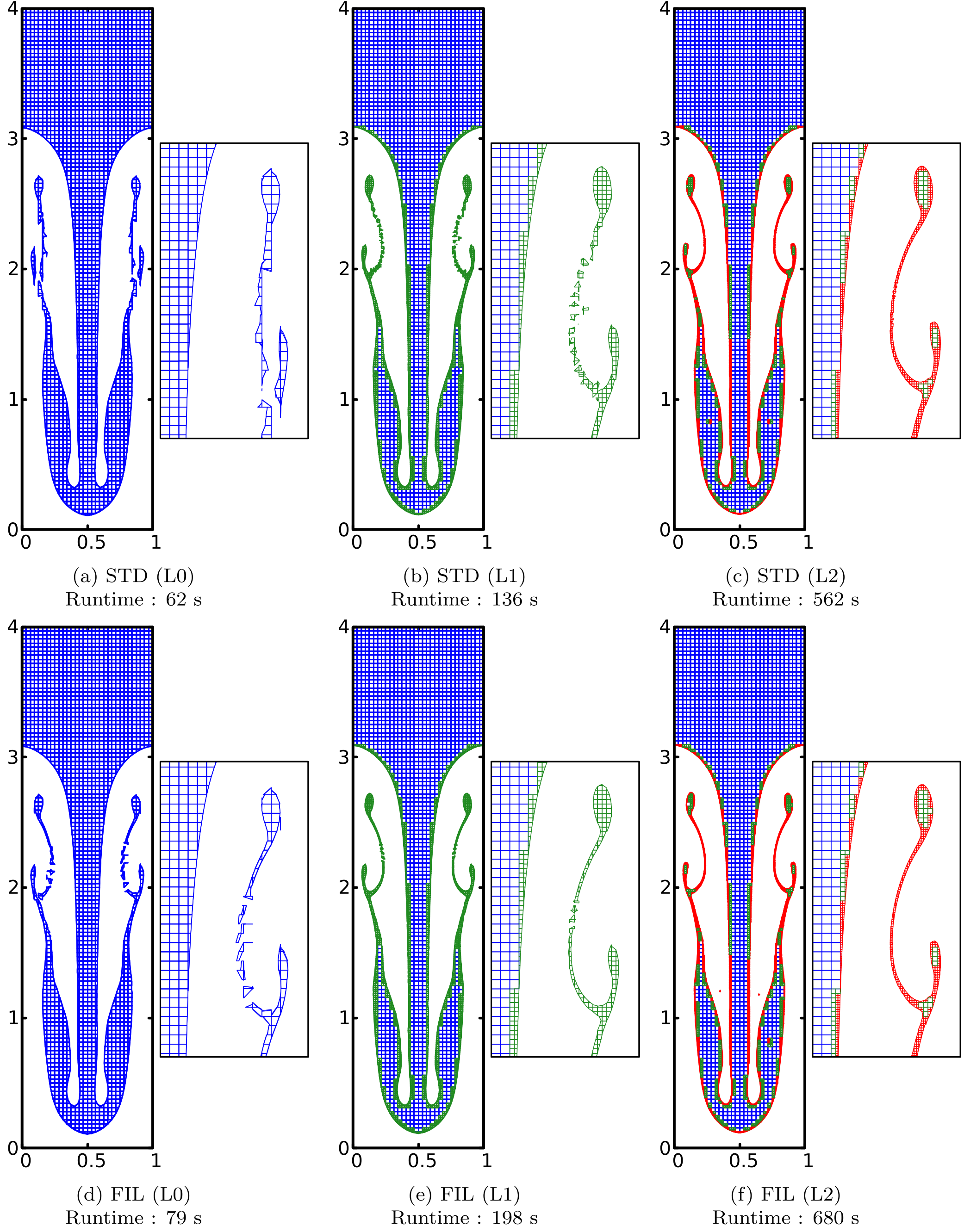

(a) STD (L0)
Runtime : 62 s

(b) STD (L1)
Runtime : 136 s

(c) STD (L2)
Runtime : 562 s

(d) FIL (L0)
Runtime : 79 s

(e) FIL (L1)
Runtime : 198 s

(f) FIL (L2)
Runtime : 680 s

Fig. 23. Study of the efficiency of the MOF-ADG method. Accuracy against refinement using both standard (STD) and filament (FIL) reconstruction. The base mesh is 32×128 and uses three different levels of refinement. The side figure shows a zoom on the tip of the filamentary mushroom, zoom box $[0.5, 1] \times [1.8, 2.8]$.

interface. The filament MOF-ADG shows a better reconstruction even on a fixed grid. Filaments do breakup with zero and one level of refinement when using a filamentary reconstruction. This can be explained by the choice of multimaterial reconstruction described in [15]. An interesting question concerns the choice of *best* variant of the MOF-ADG method in order to obtain acceptable results. On one hand, it seems that a filament method with L0 is faster and seems to breakup less than a standard MOF-ADG L1. On the other hand, a filament MOF-ADG L1 offers more breakup than the standard MOF-ADG L2, although significantly faster.

In terms of runtime, each runtime is provided in the caption, however, a conclusion cannot be drawn. The only possible comparison is the runtime between standard and filament MOF-ADG which obviously increases for the latter.

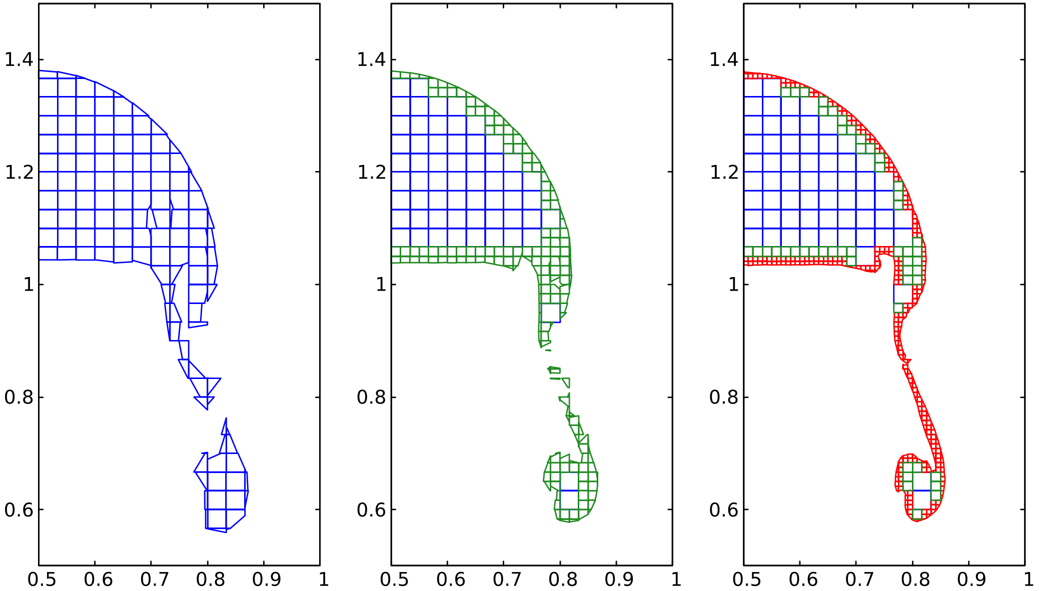

(a) STD (L0)
Runtime : 76 s

(b) STD (L1)
Runtime : 88 s

(c) STD (L2)
Runtime : 152 s

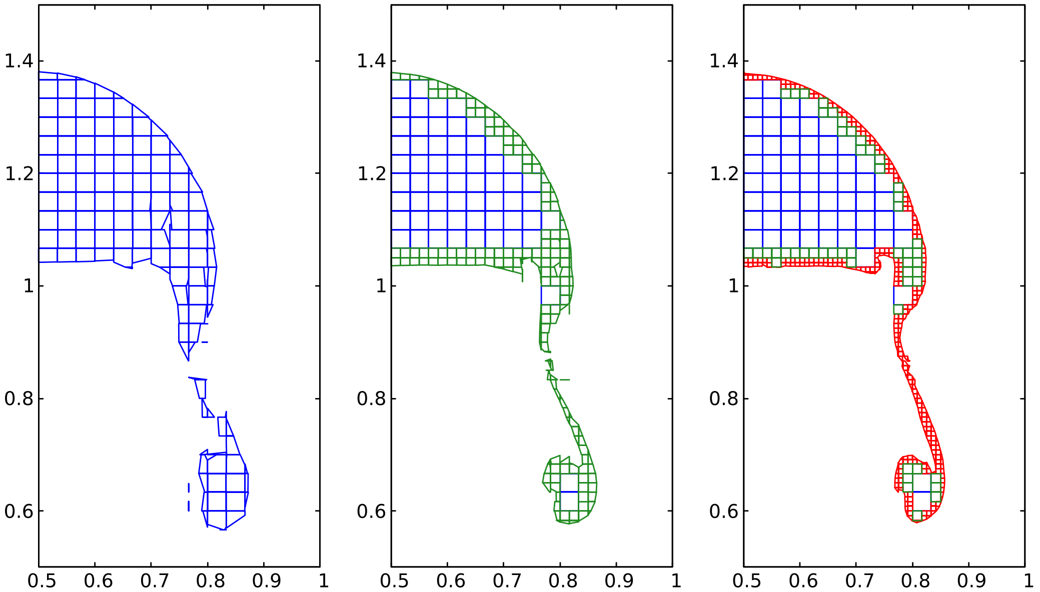

(d) FIL (L0)
Runtime : 92 s

(e) FIL (L1)
Runtime : 117 s

(f) FIL (L2)
Runtime : 160 s

Fig. 24. Bubble profile at $t = 3$ s using both standard (STD) and filament (FIL) MOF method and the dual grid method for three refinement resolution using a 30×60 base grid.

5.2. 2D rising bubble case

In this section, we provide insights into the trade-off between refinement and error using the 2D rising bubble case with surface tension modelling. The formulation of the problem and simulation setup is the same as that described in Section 4.4. In this study, we use the same 30×60 Cartesian grid with three refinement resolutions: level 0, level 1 and level 2. In addition, we use a standard MOF and a filament MOF reconstruction. The simulation is carried out until $t = 3$ s. Note the time step used in this study is different to the case shown previously. Fig. 24 presents a visual depiction of the shape of the bubble at the final stage for a standard (STD) and filament (FIL) MOF reconstruction. As the bubble rises, the interface on coarse grids forms filaments that tend to break apart due to the effects of surface tension and numerical precision. As the filamentary area is refined by our adaptive dual grid framework, the breakup behaviour is attenuated and the finest refinement tends to avoid breakup.

The refinement proposed by the adaptive dual grid approach allows us to observe the filament formation behaviour. Fig. 24 compares the interface representation of the shape of the bubble at the final stage. Runtime is also displayed in the caption. The simulation results indicate a better reconstruction of the filament leading to the satellite bubble. A shorter runtime is achieved for all cases using standard MOF, as expected, while the filament MOF method produces results with a runtime that is approximately equivalent. For this test case, the discussion of efficiency is more nuanced and the conclusion about which is the best numerical option is unclear. One could opt for a shorter runtime by using one level of refinement with filament reconstruction or choose to invest more time for better precision. While two levels of refinement offer significant improvements, the decision between using standard reconstruction or filament reconstruction is not straightforward. Spending an additional 8 seconds leads to slightly better results.

In comparison with the Rayleigh-Taylor instability, we can conclude that efficiency is highly case-dependent. Indeed, for the former, filaments appear for the majority of the simulation time, whereas for the rising bubble case, filaments only form towards the end of the simulation. The formation of filaments is the most significant factor that needs to be considered when choosing between runtime and precision.

6. Conclusions

In conclusion, this paper introduces a novel adaptive dual grid moment-of-fluid (MOF-ADG) method coupled with an implicit finite volume Navier-Stokes solver. This method represents a novel and promising approach for simulating complex multiphase flow dynamics using two separate Cartesian grids, a fixed coarse grid for the fluid solver and an adaptive grid for the interface capturing method. The present approach exhibits remarkable adaptivity in refining computational grids, offering a significant improvement in the numerical efficiency and accuracy of fluid flow simulations. In addition, numerical complexity has been enhanced by including subgrid-scale elements such as filaments in order to reduce the persisting numerical breakup of filaments through the moment-of-fluid method.

The method proposed in this study is evaluated using established benchmark problems in which there are challenges of varying complexities. The method demonstrates an excellent level of accuracy in addressing the natural sloshing problem, displaying quantitative agreement with existing literature and analytical solutions. In addition, some horizontal excitation is performed for the sloshing case. Moreover, the dam break problem successfully provides accurate quantitative estimations of water height evolution and pressure measurement, aligning well with both experimental data and previous numerical analysis for dam break flow scenarios. In the Rayleigh-Taylor instability problem, the method precisely reconstructs the interface during its early stages and effectively captures deformed subgrid-scale structures in later stages with the particularly well developed filament MOF-ADG method. In the final section, the MOF-ADG method shows its relevance within interface capturing methods by comparing reconstructions for a rising bubble exploring different refinement strategies in which the surface tension cannot be neglected. In summary, the MOF-ADG method demonstrates excellent performance in accurately capturing complex flow features and its intrinsic physical behaviour.

Despite notable progress, challenges persist in accurately capturing material diffusion within interface capturing methods such as the MOF method itself. Numerical simulations of multiphase flows using the moment-of-fluid method encounter difficulties in reconstructing sharp edges or poorly resolved structures like filament tips or tails. In addition, certain limitations of the MOF-ADG method arise notably in situations with breakup and coalescence or with extreme geometries despite offering sharper interface reconstruction. The computational expense of the proposed method is somewhat mitigated by employing analytical solutions on Cartesian grids for interface capturing features when possible. However, the use of a fixed coarse grid for the flow solver is not negligible in terms of computational efficiency. Nevertheless, this study has been carried out on a single core, leaving room for improvements through parallelisation. For our future work, the focus will be on addressing these limitations by including additional features such as fluid-structure interaction and extending the application of this method to a wider range of multiphase problems such as droplet and bubble dynamics. Furthermore, the proposed approach should be extended to three-dimensional examples. The adaptive dual grid moment-of-fluid (MOF-ADG) method has been shown to be a robust and promising enhancement to interface capturing and tracking techniques in complex numerical multiphase flows.

CRediT authorship contribution statement

Philippe Hergibo: Writing – original draft, Visualization, Validation, Software, Methodology, Investigation, Data curation. **Timothy N. Phillips:** Writing – review & editing, Supervision, Methodology, Investigation, Conceptualization. **Zhihua Xie:** Writing – review & editing, Supervision, Software, Methodology, Investigation, Funding acquisition, Conceptualization.

Declaration of competing interest

The authors declare that they have no known competing financial interests or personal relationships that could have appeared to influence the work reported in this paper.

Acknowledgements

Constructive comments from anonymous reviewers have helped to improve the manuscript and these are gratefully acknowledged. The first author would like to thank the United Kingdom Engineering and Physical Sciences Research Council (EPSRC) for providing the funding to support his doctoral study (EP/T517951/1 with project reference 2558593). Z.X. was financially supported by EPSRC grant (EP/V040235/1), The Royal Society Newton Advanced Fellowship (NAF/R1/201156) and International Exchanges Award (IEC/NSFC/211143, IES/R2/202095), and the Alexander von Humboldt Research Fellowship for experienced researchers. This research was undertaken using the supercomputing facilities at Cardiff University operated by Advanced Research Computing at Cardiff (ARCCA) and the HPC Wales and Supercomputing Wales (SCW) projects. The fruitful discussion with Professor Qiuhua Liang at Loughborough University on adaptive mesh refinement is greatly acknowledged.

Data availability

Data will be made available on request.

References

[1] C.W. Hirt, B.D. Nichols, Volume of fluid (VOF) method for the dynamics of free boundaries, J. Comput. Phys. 39 (1) (1981) 201–225.
[2] M. Rudman, A volume-tracking method for incompressible multifluid flows with large density variations, Int. J. Numer. Methods Fluids 28 (2) (1998) 357–378.
[3] M. Sussman, P. Smereka, S. Osher, A level set approach for computing solutions to incompressible two-phase flow, J. Comput. Phys. 114 (1) (1994) 146–159.
[4] V. Dyadechko, M. Shashkov, Moment-of-fluid interface reconstruction, Los Alamos Report LA-UR-05-7571, 2005, p. 49.
[5] M. Shashkov, An adaptive moments-based interface reconstruction using intersection of the cell with one half-plane, two half-planes and a circle, J. Comput. Phys. 494 (2023) 112504.
[6] A. Lemoine, S. Glockner, J. Breil, Moment-of-fluid analytic reconstruction on 2D Cartesian grids, J. Comput. Phys. 328 (2017) 131–139.
[7] T. Milcent, A. Lemoine, An analytic approach for the moment-of-fluid interface reconstruction method on tetrahedral meshes, J. Comput. Phys. (2024) 112758.
[8] R.N. Hill, M. Shashkov, The symmetric moment-of-fluid interface reconstruction algorithm, J. Comput. Phys. 249 (2013) 180–184.
[9] H.T. Ahn, M. Shashkov, Adaptive moment-of-fluid method, J. Comput. Phys. 228 (8) (2009) 2792–2821.
[10] H.T. Ahn, M. Shashkov, Multi-material interface reconstruction on generalized polyhedral meshes, J. Comput. Phys. 226 (2) (2007) 2096–2132.
[11] S.P. Schofield, M.A. Christon, V. Dyadechko, R.V. Garimella, R.B. Lowrie, B.K. Swartz, Multi-material incompressible flow simulation using the moment-of-fluid method, Int. J. Numer. Methods Fluids 63 (8) (2010) 931–952.
[12] V. Dyadechko, M. Shashkov, Reconstruction of multi-material interfaces from moment data, J. Comput. Phys. 227 (11) (2008) 5361–5384.
[13] Z. Ye, M. Sussman, Y. Zhan, X. Zhao, A decision-tree based moment-of-fluid (DTMOF) method in 3D rectangular hexahedrons, arXiv preprint, arXiv:2108.02533, 2021.
[14] M. Jemison, M. Sussman, M. Shashkov, Filament capturing with the multimaterial moment-of-fluid method, J. Comput. Phys. 285 (2015) 149–172.
[15] P. Hergibo, T.N. Phillips, Z. Xie, A moment-of-fluid method for resolving filamentary structures using a symmetric multi-material approach, J. Comput. Phys. 491 (2023) 112401.
[16] O. Desjardins, J.V. Giliberto, Z. Zou, Towards efficient and accurate modeling of pressure swirl atomization using sub-grid scale modeling of thin liquid films, in: AIAA SCITECH 2025 Forum, 2025, p. 1880.
[17] H. Ding, P.D. Spelt, C. Shu, Diffuse interface model for incompressible two-phase flows with large density ratios, J. Comput. Phys. 226 (2) (2007) 2078–2095.
[18] G. Pozzetti, H. Jasak, X. Besseron, A. Rousset, B. Peters, A parallel dual-grid multiscale approach to CFD–DEM couplings, J. Comput. Phys. 378 (2019) 708–722.
[19] K. Bazesefidpar, L. Brandt, O. Tammisola, A dual resolution phase-field solver for wetting of viscoelastic droplets, Int. J. Numer. Methods Fluids 94 (9) (2022) 1517–1541.
[20] M. Lentine, W. Zheng, R. Fedkiw, A novel algorithm for incompressible flow using only a coarse grid projection, ACM Trans. Graph. 29 (4) (2010) 1–9.
[21] V.H. Gada, A. Sharma, On a novel dual-grid level-set method for two-phase flow simulation, Numer. Heat Transf., Part B, Fundam. 59 (1) (2011) 26–57.
[22] Z. Wang, F. Stern, Volume-of-fluid based two-phase flow methods on structured multiblock and overset grids, Int. J. Numer. Methods Fluids 94 (6) (2022) 557–582.
[23] Z. Ma, L. Qian, P. Martínez-Ferrer, D. Causon, C. Mingham, W. Bai, An overset mesh based multiphase flow solver for water entry problems, Comput. Fluids 172 (2018) 689–705.
[24] A. Hay, M. Visonneau, Computation of free-surface flows with local mesh adaptation, Int. J. Numer. Methods Fluids 49 (7) (2005) 785–816.
[25] R. Biswas, J.E. Flaherty, D.C. Arney, An adaptive mesh-moving and refinement procedure for one-dimensional conservation laws, Appl. Numer. Math. 11 (4) (1993) 259–282.
[26] M. Berger, J. Oliger, Adaptive mesh refinement for hyperbolic partial differential equations, J. Comput. Phys. 53 (3) (1984) 484–512.
[27] M. Sussman, A.S. Almgren, J.B. Bell, P. Colella, L.H. Howell, M.L. Welcome, An adaptive level set approach for incompressible two-phase flows, J. Comput. Phys. 148 (1) (1999) 81–124.
[28] D. Hartmann, M. Meinke, W. Schröder, A strictly conservative Cartesian cut-cell method for compressible viscous flows on adaptive grids, Comput. Methods Appl. Mech. Eng. 200 (9–12) (2011) 1038–1052.
[29] Q. Liang, A simplified adaptive Cartesian grid system for solving the 2D shallow water equations, Int. J. Numer. Methods Fluids 69 (2) (2012) 442–458.
[30] X. Chen, V. Yang, Thickness-based adaptive mesh refinement methods for multi-phase flow simulations with thin regions, J. Comput. Phys. 269 (2014) 22–39.
[31] M. Mirzadeh, A. Guittet, C. Burstedde, F. Gibou, Parallel level-set methods on adaptive tree-based grids, J. Comput. Phys. 322 (2016) 345–364.
[32] P. Hergibo, Q. Liang, T.N. Phillips, Z. Xie, A quadtree-based adaptive moment-of-fluid method for interface reconstruction with filaments, J. Comput. Phys. 499 (2024) 112719.
[33] H.D. Ceniceros, A.M. Roma, A. Silveira-Neto, M.M. Villar, A robust, fully adaptive hybrid level-set/front-tracking method for two-phase flows with an accurate surface tension computation, Commun. Comput. Phys. 8 (1) (2010) 51–94.
[34] S. Popinet, An accurate adaptive solver for surface-tension-driven interfacial flows, J. Comput. Phys. 228 (16) (2009) 5838–5866.
[35] Z. Xie, D. Pavlidis, P. Salinas, J.R. Percival, C.C. Pain, O.K. Matar, A balanced-force control volume finite element method for interfacial flows with surface tension using adaptive anisotropic unstructured meshes, Comput. Fluids 138 (2016) 38–50.
[36] S. Banerjee, Y. Lian, Y. Liu, M. Sussman, A new method for estimating bubble diameter at different gravity levels for nucleate pool boiling, J. Heat Transf. 144 (2) (2022) 021601.
[37] A.M. Lakdawala, A. Sharma, R. Thaokar, A dual grid level set method based study on similarity and difference between interface dynamics for surface tension and radial electric field induced jet breakup, Chem. Eng. Sci. 148 (2016) 238–255.
[38] T. Patel, A. Lakdawala, A dual grid, dual level set based cut cell immersed boundary approach for simulation of multi-phase flow, Chem. Eng. Sci. 177 (2018) 180–194.
[39] D. Hartmann, M. Meinke, W. Schröder, A level-set based adaptive-grid method for premixed combustion, Combust. Flame 158 (7) (2011) 1318–1339.
[40] A.W. Woods, Turbulent plumes in nature, Annu. Rev. Fluid Mech. 42 (1) (2010) 391–412.
[41] Z. Xie, T. Stoesser, A three-dimensional Cartesian cut-cell/volume-of-fluid method for two-phase flows with moving bodies, J. Comput. Phys. 416 (2020) 109536.
[42] Z. Xie, Numerical study of breaking waves by a two-phase flow model, Int. J. Numer. Methods Fluids 70 (2) (2012) 246–268.

[43] S. Patankar, Numerical Heat Transfer and Fluid Flow, Taylor & Francis, 2018.

[44] J. Brackbill, D. Kothe, C. Zemach, A continuum method for modeling surface tension, J. Comput. Phys. 100 (2) (1992) 335–354.

[45] H.T. Ahn, M. Shashkov, M.A. Christon, The moment-of-fluid method in action, Commun. Numer. Methods Eng. 25 (10) (2009) 1009–1018.

[46] G. Li, Y. Lian, M. Sussman, Simulations of gas-liquid two-phase jet flows using the moment of fluid method, in: Fluids Engineering Division Summer Meeting, vol. 55560, American Society of Mechanical Engineers, 2013, V01CT17A014.

[47] P. Hergibo, T.N. Phillips, Z. Xie, Resolving subgrid-scale structures for multiphase flows using a filament moment-of-fluid method, Comput. Fluids 285 (2024) 106455.

[48] A. Islam, M. Sussman, H. Hu, Y. Lian, Simulation of drop impact on substrate with micro-wells, Phys. Fluids 34 (6) (2022) 062108.

[49] M. Vahab, M. Sussman, K. Shoele, Fluid-structure interaction of thin flexible bodies in multi-material multi-phase systems, J. Comput. Phys. 429 (2021) 110008.

[50] A.A. Mukundan, T. Ménard, J.C.B. de Motta, A. Berlemont, A hybrid moment of fluid–level set framework for simulating primary atomization, J. Comput. Phys. 451 (2022) 110864.

[51] A. Han, R. Chiodi, O. Desjardins, Capturing thin structures in vof simulations with two-plane reconstruction, J. Comput. Phys. 519 (2024) 113453.

[52] O. Ubbink, Numerical prediction of two fluid systems with sharp interfaces, PhD thesis, Imperial College London, 1997.

[53] D. Liu, P. Lin, A numerical study of three-dimensional liquid sloshing in tanks, J. Comput. Phys. 227 (8) (2008) 3921–3939.

[54] G. Wu, R. Eatock Taylor, D. Greaves, The effect of viscosity on the transient free-surface waves in a two-dimensional tank, J. Eng. Math. 40 (2001) 77–90.

[55] Z. Zhou, J. De Kat, B. Buchner, A nonlinear 3d approach to simulate green water dynamics on deck, in: Proceedings of the Seventh International Conference on Numerical Ship Hydrodynamics, Nantes, France, 1999, pp. 1–15.

[56] B. Buchner, Green water on ship-type offshore structures, Ph.D. thesis, Delft University of Technology Delft, The Netherlands, 2002.

[57] G. Colicchio, A. Colagrossi, M. Greco, M. Landrini, Free-surface flow after a dam break: a comparative study, Ship Technol. Res. 49 (3) (2002) 95–104.

[58] Z. Xie, D. Pavlidis, J.R. Percival, J.L. Gomes, C.C. Pain, O.K. Matar, Adaptive unstructured mesh modelling of multiphase flows, Int. J. Multiph. Flow 67 (2014) 104–110.

[59] G. Tryggvason, Numerical simulations of the Rayleigh-Taylor instability, J. Comput. Phys. 75 (2) (1988) 253–282.

[60] S. Hysing, S. Turek, D. Kuzmin, N. Parolini, E. Burman, S. Ganesan, L. Tobiska, Quantitative benchmark computations of two-dimensional bubble dynamics, Int. J. Numer. Methods Fluids 60 (11) (2009) 1259–1288.

[61] W. Doherty, T.N. Phillips, Z. Xie, A stabilised finite element framework for viscoelastic multiphase flows using a conservative level-set method, J. Comput. Phys. 477 (2023) 111936.